

# Spectral–Spatial Anti-Interference NMF for Hyperspectral Unmixing

Tingting Yang<sup>1</sup>, Meiping Song<sup>1</sup>, Member, IEEE, Sen Li<sup>1</sup>, and Yulei Wang<sup>1</sup>, Member, IEEE

**Abstract**—Hyperspectral unmixing could provide decomposition for small units in hyperspectral images (HSIs), allowing accurate analysis of ground objects. Unfortunately, interference such as noise and spectral variability prevalent in hyperspectral data poses a serious challenge for it. Accordingly, this article proposes a spectral–spatial anti-interference nonnegative matrix factorization (NMF) algorithm (SSAINMF), which improves the performance of spectral unmixing from both spectral and spatial perspectives. Specifically, the original data are analyzed and transformed into a statistical domain, where the information of each dimension can be re-expressed, followed by a proof of restricted isometric and restricted isospectral properties for endmembers and abundances between the original domain and the transformation domain. To obtain more reliable endmembers, weighting is then applied to each dimension in the transformation domain depending on the priority coefficients quantified by their contribution to data representation, with the influence of anomalous and noisy data weakened and the priorities of low-rank information emphasized. Finally, superpixels are exploited to induce local similarity and structural sparsity of abundances within the neighborhood, which reduces the sensitivity to spatial noise and spectral variability. From experimental results on synthetic and real datasets, the proposed SSAINMF has demonstrated effectiveness in decomposing mixed pixels, with better robustness.

**Index Terms**—Hyperspectral unmixing, nonnegative matrix factorization (NMF), spatial transformation, spectral variability, structural sparsity.

## I. INTRODUCTION

HYPERSPECTRAL imagery can capture hundreds or thousands of continuous spectral bands, in which all spectral data of each pixel point can be shaped into a smooth spectral curve. This is widely used to characterize different ground objects, contributing to the exploration of the Earth’s surface [1], [2].

However, the high spectral resolution of the sensor sacrifices the spatial resolution. As a result, the captured hyperspectral images (HSIs) contain a large number of mixed pixels, which adversely impacts the accurate recognition of ground objects [3]. Hyperspectral unmixing technology has attracted extensive interest.

Manuscript received 3 August 2023; revised 4 September 2023; accepted 10 September 2023. Date of publication 13 September 2023; date of current version 2 October 2023. This work was supported by the National Natural Science Foundation of China under Grant 61971082 and Grant 61890964. (Corresponding authors: Meiping Song; Yulei Wang.)

The authors are with the Center of Hyperspectral Imaging in Remote Sensing, Information Science and Technology College, Dalian Maritime University, Dalian 116026, China (e-mail: ytt5185@163.com; smping@163.com; listen@dlmu.edu.cn; wangyulei@dlmu.edu.cn).

Digital Object Identifier 10.1109/TGRS.2023.3314902

Usually, a scene is composed of several materials, and the spatial position defined by a pixel may contain more than one material, which is called a mixed pixel. Hyperspectral unmixing technology treats each mixed pixel as a weighted fusion of the pure spectra (endmembers) of all materials in the scene according to their corresponding proportions (abundances) [4], [5]. According to the mixing type, hyperspectral unmixing methods are divided into linear mixing models (LMMs) and non-LMMs (NLMM), where LMM is widely used because of its simple structure and generalization ability. In general, the LMM spectral unmixing process can be divided into two subproblems: endmember extraction (EE) and abundance estimation. Convex geometry is a popular technology for EE. It models all data points in a HSI as a convex geometry surrounded by  $P$  endmembers as  $P$  vertices. To locate these endmembers, one needs to find all  $P$  vertices that define the convex geometry. For example, pixel purity index (PPI) [6], [7], vertex component analysis (VCA) [8], N-FINDR [9], automatic target generation process (ATGP) [10], simplex growing algorithm (SGA) [11], and their improved versions. Using the extracted endmember set, the abundance estimation algorithms can count the abundance fractions of each endmember in pixels from the observed image. Typical abundance estimation algorithms include unconstrained least square (UCLS) [12], nonnegativity-constrained least square (NCLS) [13], sum-to-one constrained least square (SCLS) [14], and fully constrained least square (FCLS) [15]. But influenced by the imaging conditions, the captured HSIs are typically disturbed by external factors, meaning that the pure spectra of the materials cannot be obtained.

The blind source separation algorithm (BSS) can separate multiple blind source signals and obtain their fractions in a mixed signal without exposing a pure assumption on the source signals [16]. If the observed data, endmember set, and abundance matrix are regarded as the mixed signals, source signals, and separation matrix, respectively, then, hyperspectral unmixing can also be viewed as a classic BSS problem. Consequently, nonnegative matrix factorization (NMF) [17] with the idea of BSS has become an active topic in hyperspectral unmixing tasks. In [18], a convex geometry was embedded into NMF to improve its convergence. Guo et al. [19] extends sparse oblique-manifold to NMF, cleverly removing the physical constraints of abundance. Qian et al. [20] develops an  $L_{1/2}$  sparsity-constrained NMF ( $L_{1/2}\text{NMF}$ ) to promote the sparsity of abundances. Rajabi and Ghassanian [21]

implements a multilayer NMF (MLNMF), considering the sparsity of endmembers and abundances in each layer. To deal with the unstable solution space of NMF, a desirable method is to mine the spatial information contained within the observation data. Based on  $L_{1/2}$ NMF, Lu et al. [22] proposes a manifold regularized sparse NMF (MRSNMF), which preserves the intrinsic spatial structure for abundances. A region-based structure preserving NMF (RNMF) is designed in [23] to ensure the similarity of abundances within a subregion. Wang et al. [24] proposed a spatial group sparsity-regulated NMF (SGSNMF), which guarantees structural sparsity of abundances in a spatial group and reduces abnormal interference. In [25], NMF cooperates with the total variation to drive the smoothing of the abundance space. Under the  $L_1$ -NMF framework, Zhang et al. [26] imposes spectral–spatial weight constraints on abundance information to capture the smooth structure of the abundances.

Although NMF methods combined with spatial information can improve unmixing stability, they mainly focus on the influence of noise and variability from the spatial dimension, without full consideration of interferences from the spectral dimension. In the real HSIs, some low signal-to-noise ratio bands that are heavily damaged by water vapor and atmosphere are manually removed. It is clear that band noise and interference are ubiquitous. Relying on prior knowledge to manually remove or correct band variability is a challenging task. To solve this issue, some band-wise NMF methods [27] have been developed. For example, Wang et al. [28] developed a hyperspectral compressed sensing NMF algorithm (HCSNMF), which performs compressed sensing on the spectral dimension of the observation data and removes redundant interference such as noise. Peng et al. [29] used the reconstruction loss of each band in the iterative process to suppress band noise. In [30], an untied denoising autoencoder with sparsity (uDAS) was proposed, which uses a linear transfer function to re-represent spectral information of each band to effectively reduce band noise. The above-mentioned works pay attention to the band noise and have achieved better results. Most of them, however, only set a weighting index based on the noise contents of each band measured in the noise-corrupted data space, or linearly re-represent each band to reduce the negative impact of noise. In fact, this does not effectively separate the noise and low-rank components in the data space. As a result, it is still difficult to effectively avoid the confusion of noise and low-rank components in each dimension, which further affects the decomposition of endmembers and abundances.

Based on the fact that the signal-to-noise ratio of HSIs is relatively high, interference information contributes less to the low-order statistics of the data, but are mainly distributed in the high-order statistics. For this reason, we conduct statistics based on the correlation between the bands of the observed data, so that the low-order and high-order statistics in the observation data are distributed in different priority bands. Then, the weights are assigned for each band based on their priority coefficients to enhance the contribution of low-order statistics while weakening the influence of high-order statistics. In addition, SGSNMF constrains the structural

consistency of abundances within a spatial group and achieves better results, but it ignores the high similarity of information in the spatial group. In other words, SGSNMF can ensure that the variation trends of abundance vectors within a spatial group are consistent, but it cannot well provide a set of highly similar abundances, resulting unimpressive robustness to noise and spectral variability. To solve this issue, we not only control the variation trends of abundances within a spatial group but also limit their variation extent during optimization. In the case of ensuring that the structural consistency of the abundances in a spatial group, the similarity of the pixels in the group is also guaranteed. Such a design can effectively improve the robustness to spatial noise and spectral variability. In short, our contributions can be summarized as follows.

- 1) We develop a band-wise spectral unmixing model and proof its metric-keeping property for endmembers and abundances. The observed data domain is first transformed into a new data domain with evaluable bands, in which the statistics of the data are distributed in an orderly manner in the band dimension, and then, the weights of each dimension in the transformed domain are calculated according to their contribution to data representation. In this way, the interference of high-order statistics is weakened, and the advantages of low-order statistics are exerted to provide a more effective anti-interference ability against band noise for spectral unmixing. Furthermore, restricted isometric and restricted isospectral properties for endmembers and abundances are sequentially proved to promise consistent unmixing results.
- 2) Importantly, the low-rank component and interference component are separated in the transformed domain. The bands ranked top contains major information and can be regarded as the low-rank part of the data, and the bands ranked behind contain relatively small amounts of information, which can be regarded as the interference part. Compared with the original domain which mixes low-rank information and interference together in each band, the transformed domain separates them apart, which improves its resistance capability to spectral noise.
- 3) On the basis of 1) and 2), we also design a homogeneous constraint for all pixels within a neighborhood to develop the spectral–spatial anti-interference nonnegative matrix factorization (NMF) algorithm (SSAINMF). This idea constrains the pixel-to-pixel similarity in a neighborhood through superpixels, where all abundances in the neighborhood also satisfy structural sparsity simultaneously under the guidance of a set of inductive factors. This effectively enhances the robustness of spectral unmixing to spatial noise and spectral variability.

The rest of this article is organized as follows. Section II briefly introduces the basics of LMM and SGSNMF. Section III discusses in detail the band and spatial optimization model of the proposed work. In Section IV, the performance of the proposed work is compared and analyzed on public datasets. Section V summarizes the work of this article.

## II. RELATED WORK

### A. LMM

A scene usually has low-rank properties and is a mixture of a limited number of materials. To better understand the scene, we need to find the material types and corresponding proportions contained in each spatial position in the scene. In this case, it is necessary to use a mixing model. As a simple and effective mixing model, LMM is widely used in the field of data processing with good physical meaning. Given an observed HSI  $\mathbf{X} \in \mathbb{R}^{L \times N}$ , which contains  $N$  spatial pixels and  $L$  continuous spectral bands, the model can be defined by

$$\mathbf{X} = \mathbf{EA} + \mathbf{W} \quad (1)$$

where  $\mathbf{E} \in \mathbb{R}^{L \times P}$  is the endmember matrix with  $P$  endmember labels in total.  $\mathbf{A} = [\mathbf{a}_1, \dots, \mathbf{a}_N] \in \mathbb{R}^{P \times N}$  is the abundance matrix, representing the proportions of  $\mathbf{E}$  in each pixel.  $\mathbf{W} \in \mathbb{R}^{L \times N}$  represents the model reconstruction error. For  $\mathbf{A}$ , to meet the physical requirements, the following two properties need to be guaranteed.

- 1) Abundance nonnegative constraint (ANC):  $\mathbf{a}_i \geq \mathbf{0}, i = 1, \dots, N$ .
- 2) Abundance sum-to-one constraint (ASC):  $\mathbf{1}^T \mathbf{a}_i = 1$ .

### B. Spatial Group Sparsity Regularized NMF

NMF is a flexible LMM that can simultaneously decompose an observation data  $\mathbf{X} = [\mathbf{x}_1, \dots, \mathbf{x}_N]$  into two nonnegative matrices: basis matrix and mixture matrix. In the unmixing task, abundance and endmember matrices have the same nonnegative demand. Therefore, NMF is extended to the field of spectral unmixing. The NMF objective function is defined as follows:

$$\min_{\mathbf{E}, \mathbf{A}} \|\mathbf{X} - \mathbf{EA}\|_F^2, \quad \text{s.t. } \mathbf{E} \geq \mathbf{0}, \mathbf{A} \geq \mathbf{0}, \mathbf{1}^T \mathbf{A} = \mathbf{1}. \quad (2)$$

To improve the robustness of NMF, SGSNMF adopts the simple linear iterative clustering (SLIC) image segmentation method [34] to divide  $\mathbf{X}$  into multiple spatial groups, and ensures the structural sparsity of abundances within each spatial group. The model of SGSNMF is as follows:

$$\min_{\mathbf{E}, \mathbf{A}} \frac{1}{2} \sum_{g=1}^G \|\mathbf{X}^g - \mathbf{EA}^g\|_F^2 + \lambda \sum_{g=1}^G \sum_{\mathbf{a}_i \in \vartheta_g} d_i \|\mathbf{H}^g \mathbf{a}_i\|_2 \quad (3)$$

where  $G$  represents the number of spatial groups.  $d_i = (1/S_i^g)$  represents the confidence index of the  $i$ th pixel in the  $g$ th spatial group, and  $S_i^g$  represents the spectral–spatial distance between the  $i$ th pixel and the central pixel in the  $g$ th spatial group.  $\mathbf{H}^g$  is a diagonal weighting matrix used to promote the structural sparsity of abundances within the spatial group. Its  $p$ th value  $h_p^g = (1/\bar{h}_p^g + \varepsilon)$  on the diagonal, where  $\bar{h}_p^g$  represents the  $p$ th abundance value of the  $g$ th superpixel.  $\varepsilon$  is a fixed parameter to prevent the denominator of  $h_p^g$  from being 0. Then,  $\mathbf{E}$  and  $\mathbf{A}$  have the following gradients:

$$\text{grad } \mathbf{E} = \mathbf{EAA}^T - \mathbf{XA}^T \quad (4)$$

$$\begin{aligned} \text{grad } \mathbf{A} = & \sum_{g=1}^G (\tilde{\mathbf{E}}^T \tilde{\mathbf{E}} \mathbf{A}^g - \mathbf{E}^T \mathbf{X}^g) \\ & + \lambda \sum_{g=1}^G \sum_{\mathbf{a}_i \in \vartheta_g} d_i (\mathbf{H}^g)^T \mathbf{H}^g \mathbf{a}_i \frac{1}{\|\mathbf{H}^g \mathbf{a}_i\|_2}. \end{aligned} \quad (5)$$

In (6) and (7), the endmembers and abundances can be continuously optimized until the convergence of (3) with the step size  $\omega$  of gradient descent

$$\mathbf{E} = \max(0, \mathbf{E} - \omega \text{grad } \mathbf{E}) \quad (6)$$

$$\mathbf{A} = \max(0, \mathbf{A} - \omega \text{grad } \mathbf{A}). \quad (7)$$

## III. PROPOSED ALGORITHM: SSAINMF

### A. Spectral Optimization Model

1) *Priority-Driven Band Noise Suppression*: In hyperspectral imaging, due to the interference of external factors, the captured images contain a lot of noise, which can be viewed as band noise and spatial noise based on their performance in spectral and spatial dimensions. To effectively eliminate the interference of band noise, the data  $\mathbf{X}$  needs to be linearly transformed, separating high-order statistics that characterize anomalies and noise from low-order statistics that characterize low-rank components in all spectral bands. Specifically, as illustrated in Fig. 1,  $\mathbf{X}$  can be analyzed by correlation between bands, due to the fact that adjacent bands are continuous. First of all, the degrees of linear correlation between the bands need to be measured by

$$\Sigma = \begin{bmatrix} \sigma(\tilde{\mathbf{x}}_1 - \mu, \tilde{\mathbf{x}}_1 - \mu) & \cdots & \sigma(\tilde{\mathbf{x}}_1 - \mu, \tilde{\mathbf{x}}_L - \mu) \\ \vdots & \ddots & \vdots \\ \sigma(\tilde{\mathbf{x}}_L - \mu, \tilde{\mathbf{x}}_1 - \mu) & \cdots & \sigma(\tilde{\mathbf{x}}_L - \mu, \tilde{\mathbf{x}}_L - \mu) \end{bmatrix} \in \mathbb{R}^{L \times L} \quad (8)$$

where  $\sigma(\cdot)$  is the covariance statistical function,  $\tilde{\mathbf{x}}_l$  represents the  $l$ th band vector, and  $\mu$  is the mean band vector of  $\mathbf{X}$ . Then, decompose  $\Sigma$  to obtain a basis matrix  $\mathbf{M} \in \mathbb{R}^{L \times L}$  containing  $L$  basis vectors for spatial transformation and a priority coefficient matrix  $\mathbf{Z} \in \mathbb{R}^{L \times L}$  whose diagonal value  $z_{ll}$  represents the contribution that the  $l$ th basis vector  $\mathbf{m}_l$  can capture the effective information in  $\mathbf{X}$ . That is,

$$\Sigma = \mathbf{MZM}^T. \quad (9)$$

Now, the basis matrix  $\mathbf{M}$  satisfies: as the number  $l \rightarrow L$  of basis vectors reserved in  $\mathbf{M}$ ,  $\mathbf{M}^T \mathbf{M} \rightarrow \mathbf{I}$ .

Based on  $\mathbf{M}$ , data  $\mathbf{MX}$  in the transform domain containing  $L$  priority vectors is obtained. Among them, these priority bands are arranged in order along the spectral dimension according to the priority coefficients. This achieves the separation of high-order and low-order statistics characterized by the priority bands of the smaller and larger coefficients from  $\mathbf{X}$ . In addition, due to the differences in contributions of each priority band, they can be weighted with priority coefficients. Such an idea provides two advantages. For low-order statistics, the greater the contributions of their effective information, the larger weights are applied to them, and thus, their influence is

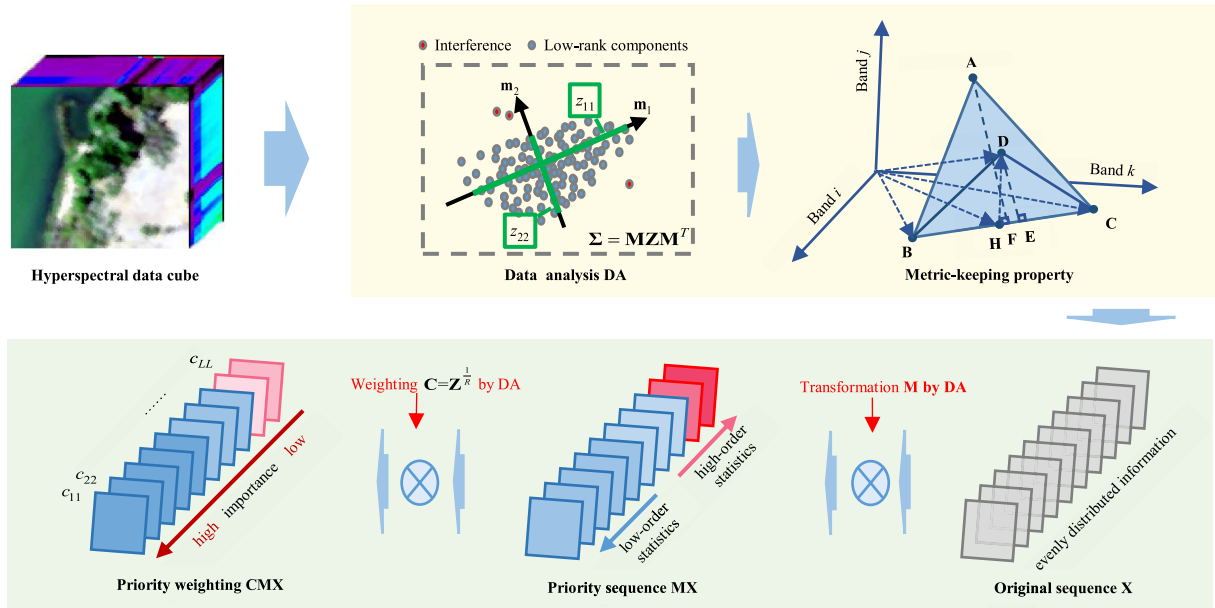


Fig. 1. Flowchart of the spatial transformation.

enhanced. For high-order statistics, the more destructive they are, the smaller weights are applied to them, thereby encouraging adaptive recovery of their corresponding valid information and suppressing their interference. However, it is worth noting that the priority coefficients of each priority band in coefficient matrix  $\mathbf{Z}$  vary greatly. The setting of weights should not only consider the influence on the spatial information but also consider the spectral information. If the gaps between adjacent weights of priority dimension are too large, the abundance will be improved, but the great loss of spectral information will result in poor endmembers. Unfortunately, the degradation of endmembers will propagate further into abundance. To balance their relationship, the weight of the  $l$ th priority band is set to  $z_{ll}^{(1/R)}$ . Let  $\mathbf{C}$  be the weighting matrix, i.e.,  $\mathbf{C} = \mathbf{Z}^{(1/R)}$ . Then, (2) can be rewritten as follows:

$$\min_{\mathbf{E}, \mathbf{A}} \|\mathbf{CM}(\mathbf{X} - \mathbf{EA})\|_F^2, \quad \text{s.t. } \mathbf{E} \geq \mathbf{0}, \mathbf{A} \geq \mathbf{0}, \mathbf{1}^T \mathbf{A} = 1. \quad (10)$$

However, a new problem arises at this time. As the data are transformed from  $\mathbf{X}$  to  $\mathbf{MX}$ , could endmembers and abundances remain consistent? Next, we will discuss it in detail.

## 2) Proof of Restricted Isospectral and Restricted Isometry Properties for Endmembers and Abundances:

a) *Restricted isospectral property for endmembers:* With the transformation matrix  $\mathbf{M}$ , (1) can be rewritten as follows:

$$\mathbf{MX} = \mathbf{MEA} + \mathbf{MW}. \quad (11)$$

Minimizing the model error  $\mathbf{MW}$ , (11) can be converted to the following optimization problem:

$$\min_{\mathbf{E}, \mathbf{A}} \|\mathbf{M}(\mathbf{X} - \mathbf{EA})\|_F^2, \quad \text{s.t. } \mathbf{E} \geq \mathbf{0}, \mathbf{A} \geq \mathbf{0}, \mathbf{1}^T \mathbf{A} = 1. \quad (12)$$

The subproblem **E** can be optimized using the gradient descent method, so we have

$$\text{grad } \hat{\mathbf{E}} = \mathbf{M}^T \mathbf{M} (\mathbf{EAA}^T - \mathbf{XA}^T). \quad (13)$$

When  $l = L$ ,  $\mathbf{M}^T \mathbf{M} \approx \mathbf{I}$ , so  $\mathbf{M}^T \mathbf{M} (\mathbf{EAA}^T - \mathbf{XA}^T) \approx (\mathbf{EAA}^T - \mathbf{XA}^T)$ . This shows that the transformation has little effect on the endmember spectrum.

b) *Restricted isometry properties for abundances:* Based on the pure pixel assumption, hyperspectral pixel points are all embedded in a simplex composed of  $P$  endmember points [31]. Considering the fact that a simplex of  $P$  vertices can be well expressed by at least a  $(P - 1)$ -dimensional data space, to fully prove the restricted isometry property of abundances, we describe its proof process in the  $(P - 1)$ - and  $P$ -dimensional data spaces, respectively. But in fact, we do not need to take any dimensionality reduction measures for the observation data during the computation of SSAINMF. Without loss of generality, we take  $P = 3$  as an example to illustrate it. First assume that the hyperspectral data  $\mathbf{X}$  contains three endmember points  $\mathbf{A}$ ,  $\mathbf{B}$ , and  $\mathbf{C}$ , and any pixel point  $\mathbf{D}$  in  $\mathbf{X}$  is located in the simplex  $ABC$  with  $\mathbf{A}$ ,  $\mathbf{B}$ , and  $\mathbf{C}$  as vertices.

i) *Proof based on simplex volume:* From the simplex  $ABC$  in Fig. 2(a), it can be known that the proportion of endmember  $\mathbf{A}_{V_{P-1}}$  in pixel  $\mathbf{D}_{V_{P-1}}$  is  $f_{\mathbf{A}_{V_{P-1}}} = (S_{BCD}^{V_{P-1}} / S_{ABC}^{V_{P-1}})$ . Considering that triangles  $BCD$  and  $ABC$  share the same side  $\mathbf{B}_{V_{P-1}} \mathbf{C}_{V_{P-1}}$ , the ratio of their areas is equivalent to the ratio of their heights with  $\mathbf{B}_{V_{P-1}} \mathbf{C}_{V_{P-1}}$  as a base, i.e.,  $f_{\mathbf{A}_{V_{P-1}}} = (|\mathbf{D}_{V_{P-1}} \mathbf{E}_{V_{P-1}}|) / (|\mathbf{A}_{V_{P-1}} \mathbf{F}_{V_{P-1}}|)$ . To obtain  $|\mathbf{D}_{V_{P-1}} \mathbf{E}_{V_{P-1}}|$  and  $|\mathbf{A}_{V_{P-1}} \mathbf{F}_{V_{P-1}}|$ , we introduce the orthogonal subspace projection (OSP) theory [32], [33] to generate the following OSP matrix of  $\mathbf{U}_{V_{P-1}} = [\mathbf{B}_{V_{P-1}}, \mathbf{C}_{V_{P-1}}]$ :

$$\mathbf{P}_{\mathbf{U}_{V_{P-1}}}^\perp = \mathbf{I} - \mathbf{U}_{V_{P-1}} (\mathbf{U}_{V_{P-1}}^T \mathbf{U}_{V_{P-1}})^{-1} \mathbf{U}_{V_{P-1}}^T. \quad (14)$$

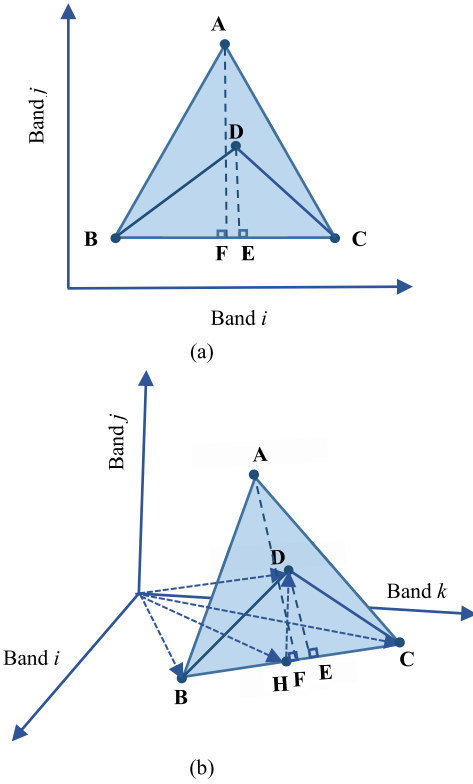


Fig. 2. Simplex  $ABC$  embedded in (a)  $(P - 1)$ -dimensional data space and (b)  $P$ -dimensional data space.

With (14), the projection vector  $\mathbf{P}_{\mathbf{U}_{V_{P-1}}}^\perp \mathbf{D}_{V_{P-1}}$  of  $\mathbf{D}_{V_{P-1}}$  on  $\mathbf{P}_{\mathbf{U}_{V_{P-1}}}^\perp$  can be obtained, so

$$\begin{aligned} & |\mathbf{D}_{V_{P-1}} \mathbf{E}_{V_{P-1}}| \\ &= \sqrt{\left(\mathbf{P}_{\mathbf{U}_{V_{P-1}}}^\perp \mathbf{D}_{V_{P-1}}\right)^T \left(\mathbf{P}_{\mathbf{U}_{V_{P-1}}}^\perp \mathbf{D}_{V_{P-1}}\right)} \\ &= \sqrt{\mathbf{D}_{V_{P-1}}^T \mathbf{D}_{V_{P-1}} - \mathbf{D}_{V_{P-1}}^T \mathbf{U}_{V_{P-1}} \left(\mathbf{U}_{V_{P-1}}^T \mathbf{U}_{V_{P-1}}\right)^{-1} \mathbf{U}_{V_{P-1}}^T \mathbf{D}_{V_{P-1}}}. \end{aligned} \quad (15)$$

Similarly, we have

$$|\mathbf{A}_{V_{P-1}} \mathbf{F}_{V_{P-1}}| = \sqrt{\left(\mathbf{P}_{\mathbf{U}_{V_{P-1}}}^\perp \mathbf{A}_{V_{P-1}}\right)^T \left(\mathbf{P}_{\mathbf{U}_{V_{P-1}}}^\perp \mathbf{A}_{V_{P-1}}\right)}. \quad (16)$$

Then, the proportion of  $\mathbf{A}$  in  $\mathbf{D}$  is

$$f_A = \frac{|\mathbf{D}_{V_{P-1}} \mathbf{E}_{V_{P-1}}|}{|\mathbf{A}_{V_{P-1}} \mathbf{F}_{V_{P-1}}|} = \frac{\sqrt{\left(\mathbf{P}_{\mathbf{U}_{V_{P-1}}}^\perp \mathbf{D}_{V_{P-1}}\right)^T \left(\mathbf{P}_{\mathbf{U}_{V_{P-1}}}^\perp \mathbf{D}_{V_{P-1}}\right)}}{\sqrt{\left(\mathbf{P}_{\mathbf{U}_{V_{P-1}}}^\perp \mathbf{A}_{V_{P-1}}\right)^T \left(\mathbf{P}_{\mathbf{U}_{V_{P-1}}}^\perp \mathbf{A}_{V_{P-1}}\right)}}. \quad (17)$$

When transforming the data space,  $\hat{\mathbf{U}}_{V_{P-1}} = \mathbf{M}\mathbf{U}_{V_{P-1}} = [\mathbf{M}\mathbf{B}_{V_{P-1}}, \mathbf{M}\mathbf{C}_{V_{P-1}}]$ , the OSP matrix becomes

$$\mathbf{P}_{\hat{\mathbf{U}}_{V_{P-1}}}^\perp = \mathbf{I} - \mathbf{M}\mathbf{U}_{V_{P-1}} \left(\mathbf{U}_{V_{P-1}}^T \mathbf{M}^T \mathbf{M} \mathbf{U}_{V_{P-1}} \mathbf{U}_{V_{P-1}}^T\right)^{-1} \mathbf{U}_{V_{P-1}}^T \mathbf{M}^T \quad (18)$$

and (19), as shown at the bottom of the next page.

In the case of the actual spectral dimension  $l = L$ ,  $\mathbf{M}^T \mathbf{M} \approx \mathbf{I}$ , so

$$\begin{aligned} & |\widehat{\mathbf{D}_{V_{P-1}} \mathbf{E}_{V_{P-1}}}| \\ & \approx \sqrt{\mathbf{D}_{V_{P-1}}^T \mathbf{D}_{V_{P-1}} - \mathbf{D}_{V_{P-1}}^T \mathbf{U}_{V_{P-1}} \left(\mathbf{U}_{V_{P-1}}^T \mathbf{U}_{V_{P-1}}\right)^{-1} \mathbf{U}_{V_{P-1}}^T \mathbf{D}_{V_{P-1}}} \\ & = |\mathbf{D}_{V_{P-1}} \mathbf{E}_{V_{P-1}}|. \end{aligned} \quad (20)$$

Similarly,  $|\widehat{\mathbf{A}_{V_{P-1}} \mathbf{F}_{V_{P-1}}}| \approx |\mathbf{A}_{V_{P-1}} \mathbf{F}_{V_{P-1}}|$ . Therefore, we can prove that  $[\hat{f}_A, \hat{f}_B, \hat{f}_C] \approx [f_A, f_B, f_C]$  before and after the data transformation.

*ii) Proof based on residual vector:* Fig. 2(b) shows the simplex  $ABC$  embedded in the 3-D space, where the proportion of  $\mathbf{A}$  in  $\mathbf{D}$  is  $f_A = (S_{BCD}/S_{ABC}) = (|\mathbf{DE}|/|\mathbf{AF}|)$ . To obtain the length of the residual vector  $|\mathbf{DE}|$  and  $|\mathbf{AF}|$ , first generate the OSP matrix of  $\mathbf{U} = \mathbf{BC} = \mathbf{C} - \mathbf{B}$  using the Gram–Schmidt orthogonalization process:

$$\mathbf{P}_{\mathbf{U}}^\perp = \mathbf{I} - \mathbf{U} (\mathbf{U}^T \mathbf{U})^{-1} \mathbf{U}^T. \quad (21)$$

Let  $\mathbf{G} = \mathbf{HD} = \mathbf{D} - (1/2)(\mathbf{B} + \mathbf{C})$ , the projection vector  $\mathbf{ED} = \mathbf{P}_{\mathbf{U}}^\perp \mathbf{G}$  of  $\mathbf{G}$  on  $\mathbf{P}_{\mathbf{U}}^\perp$  can be obtained. Therefore,

$$|\mathbf{DE}| = \sqrt{(\mathbf{P}_{\mathbf{U}}^\perp \mathbf{G})^T (\mathbf{P}_{\mathbf{U}}^\perp \mathbf{G})} = \sqrt{\mathbf{G}^T \mathbf{G} - \mathbf{G}^T \mathbf{U} (\mathbf{U}^T \mathbf{U})^{-1} \mathbf{U}^T \mathbf{G}}. \quad (22)$$

Similarly, let  $\mathbf{O} = \mathbf{HA} = \mathbf{A} - (1/2)(\mathbf{B} + \mathbf{C})$ , we have

$$|\mathbf{AF}| = \sqrt{(\mathbf{P}_{\mathbf{U}}^\perp \mathbf{O})^T (\mathbf{P}_{\mathbf{U}}^\perp \mathbf{O})}. \quad (23)$$

Then, the proportion of  $\mathbf{A}$  in  $\mathbf{D}$  is

$$f_A = \frac{|\mathbf{DE}|}{|\mathbf{AF}|} = \frac{\sqrt{(\mathbf{P}_{\mathbf{U}}^\perp \mathbf{G})^T (\mathbf{P}_{\mathbf{U}}^\perp \mathbf{G})}}{\sqrt{(\mathbf{P}_{\mathbf{U}}^\perp \mathbf{O})^T (\mathbf{P}_{\mathbf{U}}^\perp \mathbf{O})}}. \quad (24)$$

When transforming the data space,  $\hat{\mathbf{U}} = \mathbf{MU} = \mathbf{M}(\mathbf{C} - \mathbf{B})$ . The OSP matrix becomes

$$\mathbf{P}_{\hat{\mathbf{U}}}^\perp = \mathbf{I} - \mathbf{MU} (\mathbf{U}^T \mathbf{M}^T \mathbf{MU})^{-1} \mathbf{U}^T \mathbf{M}^T. \quad (25)$$

Now,  $\hat{\mathbf{G}} = \mathbf{MG} = \mathbf{M}(\mathbf{D} - (1/2)(\mathbf{B} + \mathbf{C}))$ , thereby

$$\begin{aligned} |\widehat{\mathbf{DE}}| &= \sqrt{(\mathbf{P}_{\hat{\mathbf{U}}}^\perp \mathbf{G})^T (\mathbf{P}_{\hat{\mathbf{U}}}^\perp \mathbf{G})} \\ &= \sqrt{\mathbf{G}^T \mathbf{M}^T (\mathbf{P}_{\hat{\mathbf{U}}}^\perp)^T \mathbf{P}_{\hat{\mathbf{U}}}^\perp \mathbf{M} \mathbf{G}} \\ &= \sqrt{\mathbf{G}^T \mathbf{M}^T \mathbf{P}_{\hat{\mathbf{U}}}^\perp \mathbf{M} \mathbf{G}} \\ &= \sqrt{\mathbf{G}^T \mathbf{M}^T (\mathbf{I} - \mathbf{MU} (\mathbf{U}^T \mathbf{M}^T \mathbf{MU})^{-1} \mathbf{U}^T \mathbf{M}^T)) \mathbf{M} \mathbf{G}} \\ &= \sqrt{\mathbf{G}^T \mathbf{M}^T \mathbf{M} \mathbf{G} - \mathbf{G}^T \mathbf{M}^T \mathbf{M} \mathbf{U} (\mathbf{U}^T \mathbf{M}^T \mathbf{M} \mathbf{U})^{-1} \mathbf{U}^T \mathbf{M}^T \mathbf{M} \mathbf{G}}. \end{aligned} \quad (26)$$

Because of  $l = L$ ,  $\mathbf{M}^T \mathbf{M} \approx \mathbf{I}$ . Thus,

$$|\widehat{\mathbf{DE}}| \approx \sqrt{\mathbf{G}^T \mathbf{G} - \mathbf{G}^T \mathbf{U} (\mathbf{U}^T \mathbf{U})^{-1} \mathbf{U}^T \mathbf{G}} = |\mathbf{DE}|. \quad (27)$$

Similarly,  $|\widehat{\mathbf{AF}}| \approx |\mathbf{AF}|$ . Based on this, we can prove that  $[\hat{f}_A, \hat{f}_B, \hat{f}_C] \approx [f_A, f_B, f_C]$  before and after the spatial transformation.

### B. Spatial Optimization Model

In most cases, adjacent pixels are usually composed of similar materials, so the effective exploration of local spatial information can better improve the unmixing performance and eliminate interference such as spatial noise and spectral variability. Using SLIC image segmentation [24], a scene can be divided into  $S$  local neighborhoods. Considering the homogeneity of pixels in a neighborhood, we first constrain the similarity between pixels within the  $s$ th neighborhood  $\Omega_s$  using the abundance  $\mathbf{a}_s^*$  of the  $s$ th superpixel by

$$\min_{\mathbf{A}} g(\mathbf{A}) = \lambda \sum_{s=1}^S \sum_{\mathbf{a}_j \in \Omega_s} \|\mathbf{a}_j - \mathbf{a}_s^*\|_2^2 \quad (28)$$

where  $\lambda$  is a regular term that controls the influence of  $g(\mathbf{A})$ , and  $\mathbf{a}_j$  is the  $j$ th abundance in  $\Omega_s$ . Since the pixels in the subregion are not exactly the same, the pixels near the center of the subregion are more similar to the superpixel of the subregion, while the edge pixels are less similar. Therefore, we need to adjust the similarity strength between pixels in  $\Omega_s$  according to their spectral–spatial distance  $\mathbf{v}_j$  [24] from their superpixel, and (28) becomes

$$\min_{\mathbf{A}} g(\mathbf{A}) = \lambda \sum_{s=1}^S \sum_{\mathbf{a}_j \in \Omega_s} \mathbf{d}_j \|\mathbf{a}_j - \mathbf{a}_s^*\|_2^2 \quad (29)$$

where  $\mathbf{d}_j = (1/\mathbf{v}_j) = (1/(d_s^2 + (d_s^2/\omega)^2 \omega_s^2)^{1/2})$  represents the similarity index of the  $j$ th pixel in  $\Omega_s$ ,  $d_s$  and  $d_s$  are the spectral angle distance (SAD) and Euclidean distance between the  $j$ th pixel in  $\Omega_s$  and superpixel of  $\Omega_s$ , respectively,  $\omega_s$  is used to balance the influence of spectrum and spatial distance on  $\mathbf{d}_j$ , and the superpixel size  $\omega$  is used to calculate the total number of superpixels in the data.

Furthermore, the abundances in the local neighborhood should have structural sparsity. To promote this structural sparsity by endmember, we focus on the endmember  $\mathbf{e}_p$  with the highest content in the neighborhood. Its any abundance  $a_{pj}$  in the neighborhood should be given a small weight  $w_p^s$ . Based on the minimization criterion,  $a_{pj}$  will get larger to get close to the abundance  $a_{sp}^*$  of  $\mathbf{e}_p$  in  $\mathbf{a}_s^*$ . Conversely, the endmember with the lowest content within the neighborhood is given a large weight to all its abundances, making them smaller. Therefore, we extend (29) to

$$\min_{\mathbf{A}} g(\mathbf{A}) = \lambda \sum_{s=1}^S \sum_{\mathbf{a}_j \in \Omega_s} \mathbf{d}_j \|\mathbf{W}^s \mathbf{a}_j - \mathbf{a}_s^*\|_2^2 \quad (30)$$

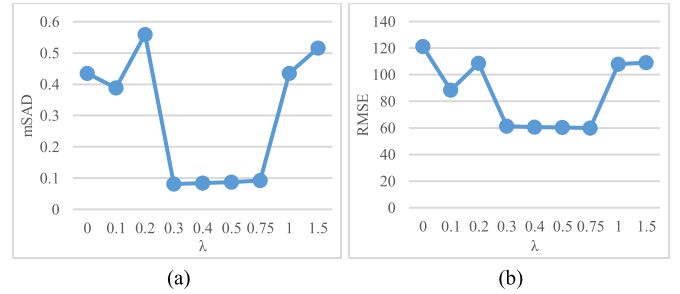


Fig. 3. Performance analysis of the proposed SSAINMF with different  $\lambda$ . (a) mSAD. (b) RMSE.

where  $\mathbf{W}^s = \text{diag}([w_1^s, \dots, w_p^s, \dots, w_P^s]) = \text{diag}(1/(\mathbf{a}_s^* + P - 3 + \varepsilon))$  is the inducing matrix for controlling the structural sparsity of the abundances in  $\Omega_s$ . A scene with more endmembers is relatively more complicated. This makes the abundances within its subregions tend to have weaker structural sparsity. Therefore, the number  $P$  of endmembers is used to control the structural sparsity.

### C. Final Proposed Model (SSAINMF)

In this way, a spectral–spatial anti-interference NMF for hyperspectral unmixing (SSAINMF) is proposed by extending (30) into (10), which can effectively resist interferences such as noise and spectral variability from the 3-D of spectrum and space. Consequently, the final objective function of SSAINMF is

$$\begin{aligned} \min_{\mathbf{E}, \mathbf{A}} f(\mathbf{E}, \mathbf{A}) &= \| \mathbf{C} \mathbf{M} (\mathbf{X} - \mathbf{E} \mathbf{A}) \|_F^2 \\ &+ \lambda \sum_{s=1}^S \sum_{\mathbf{a}_j \in \Omega_s} \mathbf{d}_j \|\mathbf{W}^s \mathbf{a}_j - \mathbf{a}_s^*\|_2^2 \\ \text{s.t. } \mathbf{E} &\geq \mathbf{0}, \mathbf{A} \geq \mathbf{0}, \mathbf{1}^T \mathbf{A} = \mathbf{1}. \end{aligned} \quad (31)$$

### D. Solution of SSAINMF

Since (31) contains two joint variables  $\mathbf{E}$  and  $\mathbf{A}$ , the subproblems  $\mathbf{E}$  and  $\mathbf{A}$  can be solved alternately by NMF

$$\mathbf{E} = \arg \min_{\mathbf{E}, \mathbf{A}} f(\mathbf{E}, \mathbf{A}) = \max(0, \mathbf{E} - \alpha \text{ grad } \mathbf{E}) \quad (32)$$

$$\mathbf{A} = \arg \min_{\mathbf{E}, \mathbf{A}} f(\mathbf{E}, \mathbf{A}) = \max(0, \mathbf{A} - \alpha \text{ grad } \mathbf{A}) \quad (33)$$

where  $\alpha$  represents the step size of gradient descent, and the gradients of  $\mathbf{E}$  and  $\mathbf{A}$  in (31) are as follows:

$$\text{grad } \mathbf{A} = \mathbf{E}^T \mathbf{M}^T \mathbf{C}^T \mathbf{C} \mathbf{M} \mathbf{E} \mathbf{A} - \mathbf{E}^T \mathbf{M}^T \mathbf{C}^T \mathbf{C} \mathbf{M} \mathbf{X} \quad (34)$$

$$\begin{aligned} \widehat{\mathbf{D}_{V_{P-1}} \mathbf{E}_{V_{P-1}}} &= \sqrt{\left( \mathbf{P}_{\tilde{\mathbf{U}}_{V_{P-1}}}^\perp \mathbf{M} \mathbf{D}_{V_{P-1}} \right)^T \left( \mathbf{P}_{\tilde{\mathbf{U}}_{V_{P-1}}}^\perp \mathbf{M} \mathbf{D}_{V_{P-1}} \right)} \\ &= \sqrt{\mathbf{D}_{V_{P-1}}^T \mathbf{M}^T \left( \mathbf{P}_{\tilde{\mathbf{U}}_{V_{P-1}}}^\perp \right)^T \mathbf{P}_{\tilde{\mathbf{U}}_{V_{P-1}}}^\perp \mathbf{M} \mathbf{D}_{V_{P-1}}} = \sqrt{\mathbf{D}_{V_{P-1}}^T \mathbf{M}^T \mathbf{P}_{\tilde{\mathbf{U}}_{V_{P-1}}}^\perp \mathbf{M} \mathbf{D}_{V_{P-1}}} \\ &= \sqrt{\mathbf{D}_{V_{P-1}}^T \mathbf{M}^T \left( \mathbf{I} - \mathbf{M} \mathbf{U}_{V_{P-1}} \left( \mathbf{U}_{V_{P-1}}^T \mathbf{M}^T \mathbf{M} \mathbf{U}_{V_{P-1}} \right)^{-1} \mathbf{U}_{V_{P-1}}^T \mathbf{M}^T \right) \mathbf{M} \mathbf{D}_{V_{P-1}}} \\ &= \sqrt{\mathbf{D}_{V_{P-1}}^T \mathbf{M}^T \mathbf{M} \mathbf{D}_{V_{P-1}} - \mathbf{D}_{V_{P-1}}^T \mathbf{M}^T \mathbf{M} \mathbf{U}_{V_{P-1}} \left( \mathbf{U}_{V_{P-1}}^T \mathbf{M}^T \mathbf{M} \mathbf{U}_{V_{P-1}} \right)^{-1} \mathbf{U}_{V_{P-1}}^T \mathbf{M}^T \mathbf{M} \mathbf{D}_{V_{P-1}}} \end{aligned} \quad (19)$$

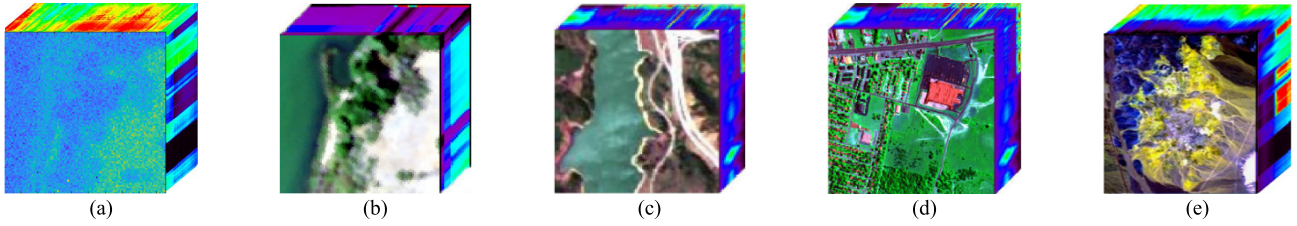


Fig. 4. False-color images of (a) synthetic data, (b) Samson, (c) Jasper Ridge, (d) urban, and (e) cuprite.

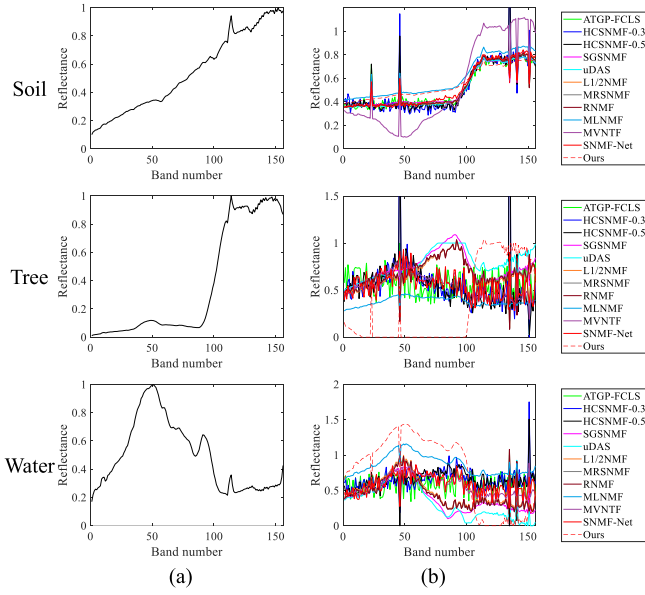


Fig. 5. Estimated endmember spectra by all tested algorithms with Synthetic data. (a) True. (b) Estimate.

$$+ \lambda \sum_{s=1}^S \sum_{\mathbf{a}_j \in \Omega_s} \mathbf{d}_j \mathbf{W}^{sT} (\mathbf{W}^s \mathbf{a}_j - \mathbf{a}_s^*) \\ \text{grad } \mathbf{E} = \mathbf{M}^T \mathbf{C}^T \mathbf{CM} \mathbf{E} \mathbf{A}^T - \mathbf{M}^T \mathbf{C}^T \mathbf{CM} \bar{\mathbf{X}}^T. \quad (35)$$

Furthermore, to guarantee the ASC of  $\mathbf{A}$ , the matrices  $\mathbf{X}$  and  $\mathbf{E}$  need to be expanded as follows:

$$\bar{\mathbf{X}} = \begin{bmatrix} \mathbf{X} \\ \beta \mathbf{1}_N^T \end{bmatrix}, \quad \bar{\mathbf{E}} = \begin{bmatrix} \mathbf{E} \\ \beta \mathbf{1}_P^T \end{bmatrix} \quad (36)$$

where  $\beta$  is a positive value used to enhance the ASC for  $\mathbf{A}$ . In our experiments, it is set to 15. Therefore, (34) becomes

$$\text{grad } \mathbf{A} = \bar{\mathbf{E}}^T \mathbf{M}^T \mathbf{C}^T \mathbf{CM} \bar{\mathbf{E}} - \bar{\mathbf{E}}^T \mathbf{M}^T \mathbf{C}^T \mathbf{CM} \bar{\mathbf{X}} \\ + \lambda \sum_{s=1}^S \sum_{\mathbf{a}_j \in \Omega_s} \mathbf{d}_j \mathbf{W}^{sT} (\mathbf{W}^s \mathbf{a}_j - \mathbf{a}_s^*). \quad (37)$$

Alternately update (32) and (33) until (31) converges to a local minimum, then the optimal set of endmembers and abundances can be obtained. Please refer to Algorithm 1 for details.

#### IV. EXPERIMENTAL ANALYSIS

To fully verify the performance of SSAINMF, the state-of-the-art correlation algorithms ATGP-FCLS [10], [15], HCSNMF [28], SGSNMF [24], uDAS [30],  $L_{1/2}$ NMF [20], MRSNMF [22], RNMF [23], MLNMF [21], matrix-vector

---

#### Algorithm 1 Summary of SSAINMF

---

**Input:**  $\mathbf{X}$ ,  $P$ ,  $\lambda$ ,  $\omega$ ,  $\omega_s$ ,  $\epsilon$

**Pre-processing:**

Generate  $\mathbf{C}$  and  $\mathbf{M}$  by (9) and  $\mathbf{C} = \mathbf{Z}^{\frac{1}{R}}$ .

Initialize  $\mathbf{E}$  and  $\mathbf{A}$  based on ATGP and FCLS.

Generate  $S$  local neighborhood based on SLIC.

Calculate the similarity index  $\mathbf{d}_j$ .

**Repeat until convergence:**

Update the inducing matrix  $\mathbf{W}^s = \text{diag}(\frac{1}{\mathbf{a}_s^* + P - 3 + \epsilon})$

Update the augmented matrices  $\bar{\mathbf{X}}$  and  $\bar{\mathbf{E}}$  by (36).

Update the abundance matrix  $\mathbf{A}$  by (33) and (37).

Update the endmember matrix  $\mathbf{E}$  by (32) and (35).

**Output:**  $\mathbf{E}$ ,  $\mathbf{A}$ .

---

nonnegative tensor factorization (MVNTF) [35], and learning a deep alternating neural network for hyperspectral unmixing (SNMF-Net) [36] are selected for comparative experiments on synthetic and real datasets, where HCSNMF includes five cases with sampling rates of 0.1, 0.2, 0.3, 0.4, and 0.5. From HCSNMF, the best two cases with sampling rates of 0.3 and 0.5, named as HCSNMF-0.3 and HCSNMF-0.5, respectively, are selected for comparison. To ensure that all tested algorithms have the same initial settings, their initial endmembers and abundances are generated by ATGP and FCLS, and their maximum number of iterations is set to 100. Furthermore, the performance of each algorithm is objectively evaluated using three evaluation criteria: normalized mean square error (NMSE), root mean square error (RMSE), and spectral angle distance (SAD). They can be expressed as follows:

$$\text{NMSE} = \frac{\|\mathbf{X} - \hat{\mathbf{X}}\|_F^2}{\|\mathbf{X}\|_F^2} \quad (38)$$

$$\text{RMSE} = \left( \frac{1}{N} \|\mathbf{A} - \hat{\mathbf{A}}\|_F^2 \right)^{\frac{1}{2}} \quad (39)$$

$$\text{SAD} = \arccos \left( \frac{\mathbf{e}_p^T \hat{\mathbf{e}}_p}{\|\mathbf{e}_p\| \|\hat{\mathbf{e}}_p\|} \right) \quad (40)$$

where  $\mathbf{X}$  represents the original image, and  $\hat{\mathbf{X}}$  represents the reconstructed image.  $\mathbf{A}$  denotes the reference abundances, and  $\hat{\mathbf{A}}$  denotes the estimated abundances,  $\mathbf{e}_p$  represents the  $p$ th reference endmember, and  $\hat{\mathbf{e}}_p$  represents the  $p$ th estimated endmember. To emphasize the comparison effects between all tested algorithms, we will bold the first-ranked score, and underline the second-ranked score.

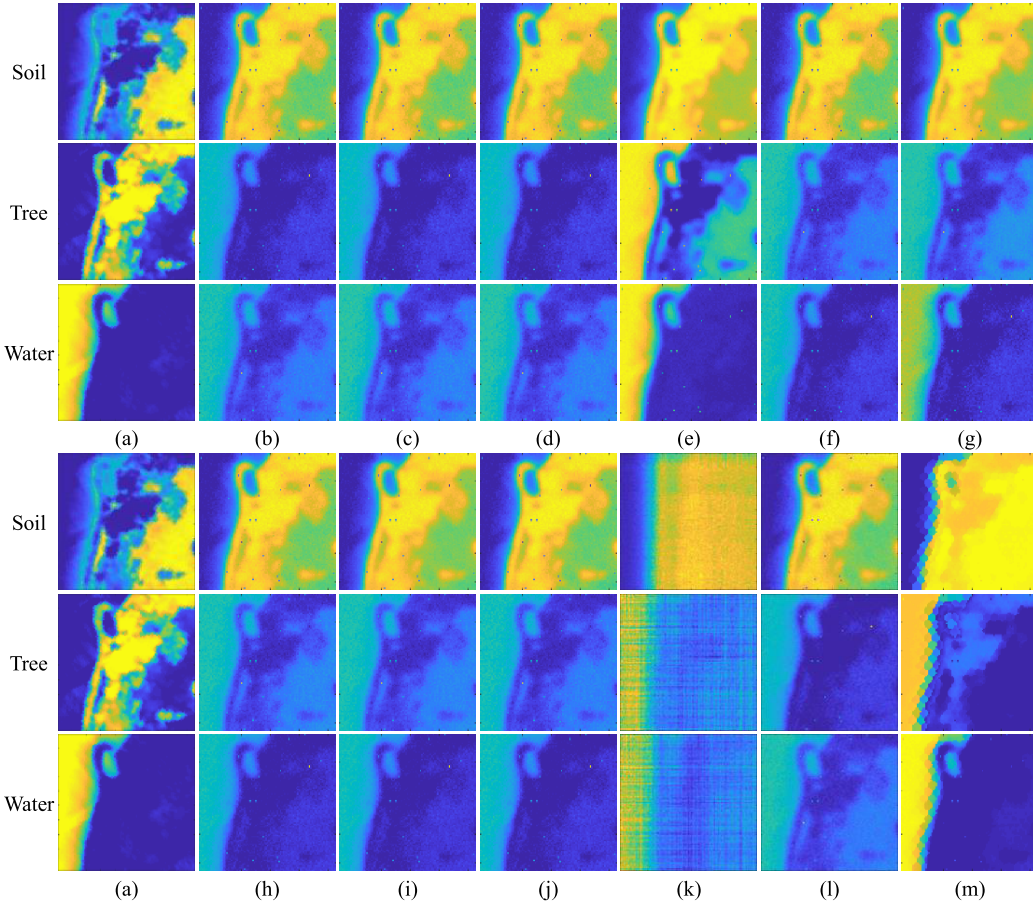


Fig. 6. Abundance maps evaluated by all tested algorithms from synthetic data. (a) True. (b) ATGP-FCLS. (c) HCSNMF-0.3. (d) HCSNMF-0.5. (e) SGSNMF. (f) uDAS. (g)  $L_{1/2}$ NMF. (h) MRSNMF. (i) RNMF. (j) MLNMF. (k) MVNTF. (l) SNMF-Net. (m) Ours.

TABLE I  
COMPARISON RESULTS OF ALL TESTED ALGORITHMS WITH SYNTHETIC DATA

	NMSE( $\times 10^{-2}$ )	RMSE	SAD			MSAD
			Soil	Tree	Water	
ATGP-FCLS [10], [15]	2.0506	114.4520	0.2379	0.8703	0.4845	0.5309
HCSNMF-0.3 [28]	0.3930	114.3441	0.2938	1.0187	0.4882	0.6002
HCSNMF-0.5 [28]	0.3912	114.4072	0.2769	1.0568	0.4607	0.5981
SGSNMF [24]	<b>0.3417</b>	115.2746	0.2281	0.8861	0.3338	0.4826
uDAS [30]	0.4323	111.0400	0.2214	<b>0.8057</b>	0.4197	0.4822
$L_{1/2}$ NMF [20]	<b>0.3661</b>	<b>109.6283</b>	0.2194	0.8833	0.3065	0.4697
MRSNMF [22]	0.3942	110.9315	0.2204	0.8732	0.3134	0.4690
RNMF [23]	0.3965	110.1697	<b>0.2190</b>	0.8815	0.3162	0.4722
MLNMF [21]	1.1759	111.7223	0.2371	0.8620	<b>0.3034</b>	<b>0.4675</b>
MVNTF [35]	0.7605	<b>91.0388</b>	0.2730	0.9888	<b>0.2597</b>	0.5072
SNMF-Net [36]	0.5126	114.6193	<b>0.2073</b>	0.9411	0.3425	0.4969
Ours	0.4384	111.0911	0.2652	<b>0.2412</b>	0.3072	<b>0.2712</b>

### A. Parameter Analysis

A first confirmation is required for parameter  $\lambda$ , which is used to balance the effect of spatial constraint in SSAINMF. Fig. 3(a) and (b) shows the change trends of endmember and abundance performance obtained by SSAINMF with the increase of  $\lambda$  on Samson, respectively. It can be observed that when  $\lambda$  is in the range [0.3, 0.75], the unmixing results of SSAINMF are relatively stable, and the effects are better. When it is beyond this range, the unmixing results become

significantly worse. Therefore, in our experiment, we set  $\lambda$  uniformly to 0.3.

### B. Experiments on Synthetic Data

In Fig. 4(a), a  $95 \times 95$  synthetic data with 156 bands is generated using the ground truth endmembers and abundances in Samson to evaluate the performance of the proposed SSAINMF. A Gaussian filter is used to smooth the synthetic data. Moreover, to approach the real situation, a certain amount

TABLE II  
COMPARISON RESULTS OF ALL TESTED ALGORITHMS WITH SAMSON DATA

	NMSE ( $\times 10^{-2}$ )	RMSE	SAD			MSAD
			Soil	Tree	Water	
ATGP-FCLS [10], [15]	124.1096	123.0139	0.0404	<b>0.0219</b>	1.0948	0.3857
HCSNMF-0.3 [28]	<u>0.1866</u>	82.9384	0.0372	0.0725	1.2191	0.4429
HCSNMF-0.5 [28]	<b>0.1649</b>	123.2034	<u>0.0358</u>	0.0333	1.1074	0.3921
SGSNMF [24]	0.2273	<u>81.2318</u>	0.9694	0.0341	0.4137	0.4724
uDAS [30]	14.0622	93.9539	0.1272	0.1613	0.3212	0.2032
L1/2NMF [20]	0.6058	88.8268	0.0586	0.0848	0.3111	<u>0.1515</u>
MRSNMF [22]	4.7215	111.3703	0.2666	0.0883	0.3204	0.2251
RNMF [23]	4.7086	110.3499	0.2612	0.1039	0.3261	0.2304
MLNMF [21]	15.2281	119.3419	0.3486	<u>0.0311</u>	0.3197	0.2331
MVNNTF [35]	2.4237	97.5289	0.2186	0.1615	0.2558	0.2120
SNMF-Net [36]	3.1291	86.8129	0.6937	0.1641	<b>0.1013</b>	0.3197
Ours	1.1112	<b>61.2956</b>	<b>0.0153</b>	0.0325	<u>0.1958</u>	<u>0.0812</u>

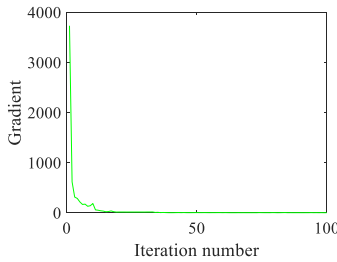


Fig. 7. Convergence curve of our SSAINMF on synthetic data.

of band noise, pixel noise, and Gaussian white noise are added to it. Then, the performance of all tested algorithms is evaluated on the synthetic data.

From Fig. 5, all algorithms have achieved better Soil endmembers. For Water endmember, MVNTF, SGSNMF, uDAS,  $L_{1/2}$ NMF, MRSNMF, RNMF, MLNMF, SNMF-Net, and Ours with sparse constraints have better performance, which proves that sparse constraint of abundances can further improve endmembers. However, most algorithms fail to obtain the tree endmembers, only our algorithm is close to the reference value. In Fig. 6, SGSNMF,  $L_{1/2}$ NMF, MVNTF, and Ours obtain better Water abundances, but poor soil and tree abundances.

Table I measures the unmixing performance of each algorithm. It can be observed that most algorithms have obtained poor endmembers and abundances. Although the abundance error of our SSAINMF is 22% higher than that of MVNTF, its reconstruction and endmember errors are 42% and 47% lower than MVNTF, respectively, providing better performance.

Fig. 7 shows the convergence curve of the proposed SSAINMF on the Synthetic data. The gradient decreases quickly at the beginning and becomes stable after 20 iterations.

### C. Experiments on Real Data

All tested algorithms are then tested on four public data shown in Fig. 4(b)–(e), Samson, Jasper Ridge, urban, and cuprite. First, a brief introduction to each data is given:

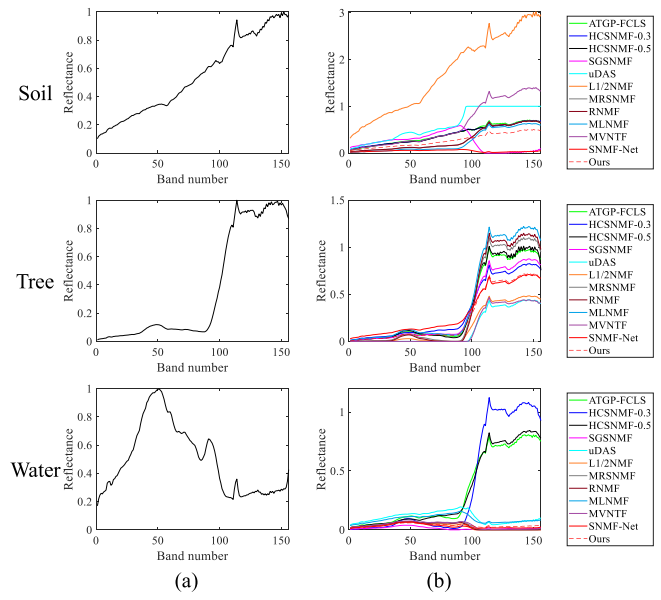


Fig. 8. Estimated endmember spectra by all tested algorithms from Samson data. (a) True. (b) Estimate.

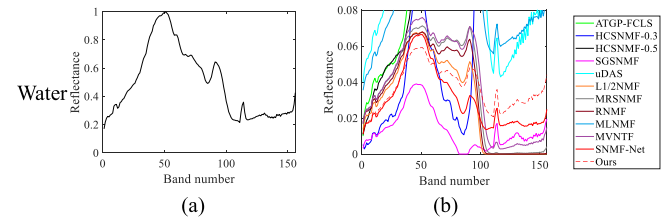


Fig. 9. Enlarged spectral curves of estimated water endmembers on Samson data. (a) True. (b) Estimate.

**Samson:** Samson originally has  $952 \times 952$  pixels that contained 156 bands spanning 401–889-nm wavelengths with a 3.13-nm spectral resolution. From its (252, 332)th pixel, a  $95 \times 95$  subregion, as shown in Fig. 4(b), is cropped. All bands in the image are reserved since there are no severely damaged bands. Moreover, it contains three materials in total: soil, tree, and water.

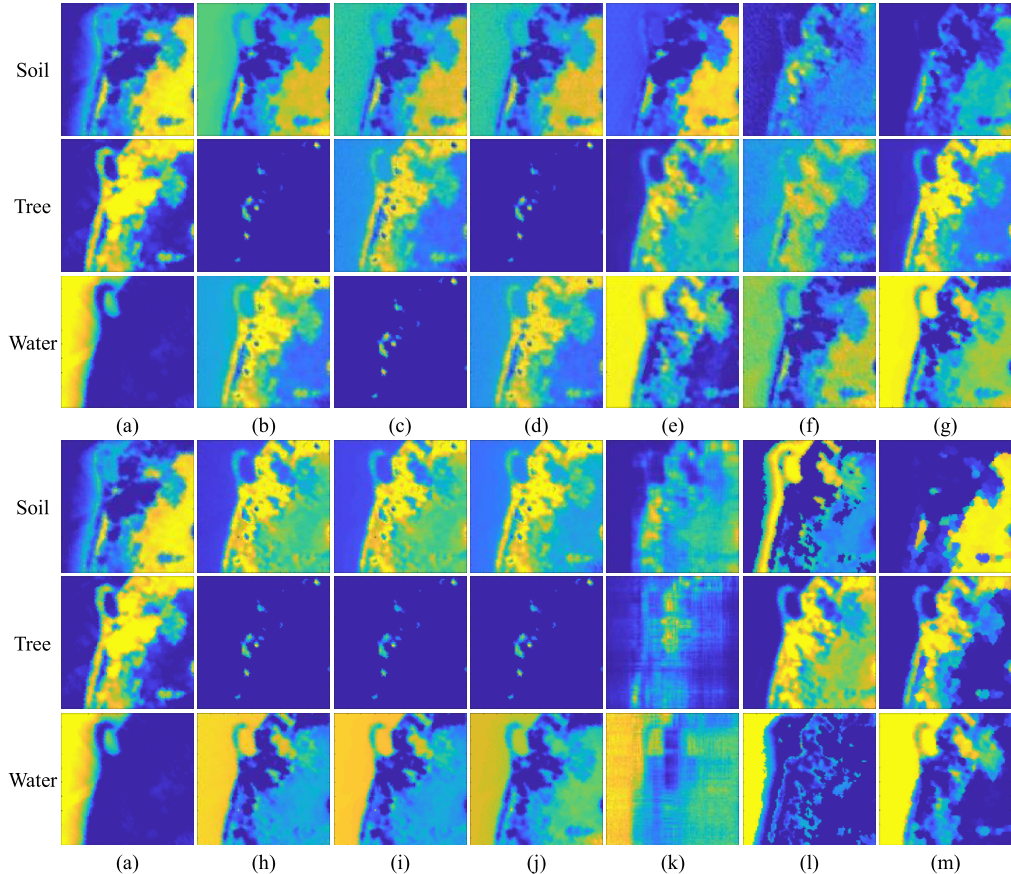


Fig. 10. Abundance maps evaluated by all tested algorithms from Samson data. (a) True. (b) ATGP-FCLS. (c) HCSNMF-0.3. (d) HCSNMF-0.5. (e) SGSNMF. (f) uDAS. (g)  $L_{1/2}$ NMF. (h) MRSNMF. (i) RNMF. (j) MLNMF. (k) MVNTF. (l) SNMF-Net. (m) Ours.

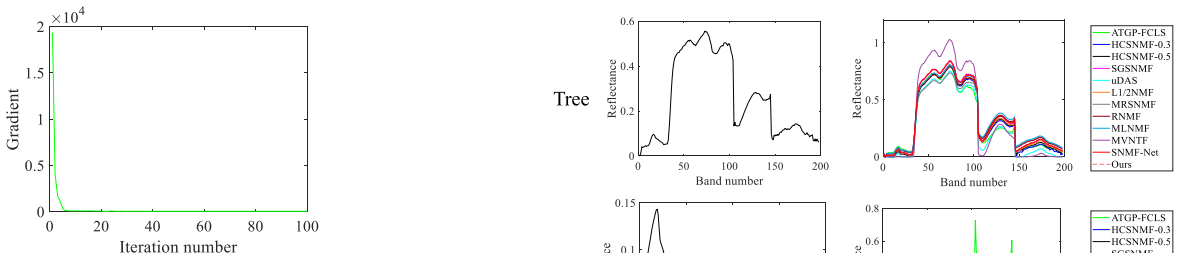


Fig. 11. Convergence curve of our SSAINMF on Samson data.

**Jasper Ridge:** Jasper ridge contains  $512 \times 614$  pixels with a wavelength range of 380–2500 nm, divided into 224 bands at a spectral resolution of 9.46 nm. Considering the ground truth of Jasper Ridge is difficult to label. Starting from its (105, 269)th pixel, a  $100 \times 100$  subimage, as shown in Fig. 4(c), is obtained. Due to water vapor and atmospheric interference, the abnormal bands 1–3, 108–112, 154–166, and 220–224 are removed, leaving 198 bands. The data mainly consists of four materials: road, soil, water, and tree.

**Urban:** Urban data in Fig. 4(d) contains  $307 \times 307$  pixels with a wavelength range of 400–2500 nm. Based on 10-nm spectral resolution, it is divided into 210 bands. After removing the heavily noisy bands 1–4, 76, 87, 101–111, 136–153, and 198–210, the 162 channels with higher SNR are retained. In the scene, there are four materials: asphalt, grass, tree, and roof.

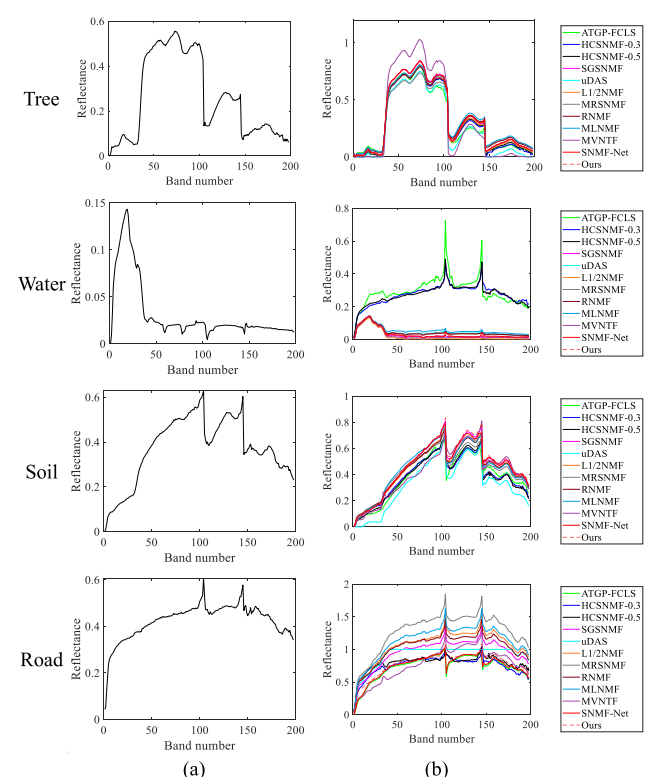


Fig. 12. Endmember curves evaluated by each algorithm on the Jasper Ridge data. (a) True. (b) Estimate.

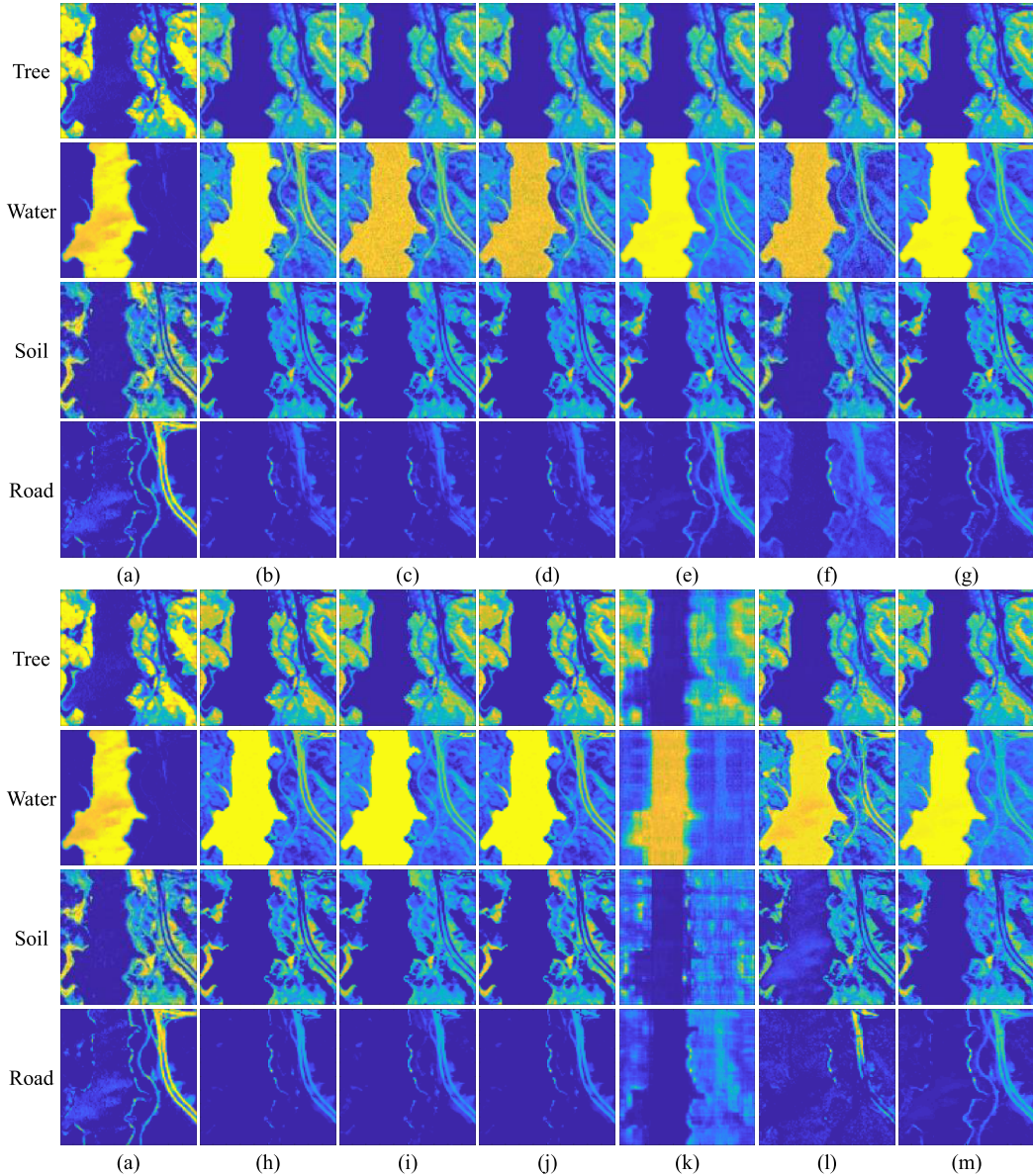


Fig. 13. Abundance maps evaluated by all tested algorithms with Jasper Ridge data. (a) True. (b) ATGP-FCLS. (c) HCSNMF-0.3. (d) HCSNMF-0.5. (e) SGSNMF. (f) uDAS. (g)  $L_{1/2}$ NMF. (h) MRSNMF. (i) RNMF. (j) MLNMF. (k) MVNTF. (l) SNMF-Net. (m) Ours.

*Cuprite:* Cuprite data shown in Fig. 4(e) has a total of  $250 \times 190$  pixels with 224 bands ranging from 370 to 2480 nm.

Since the damaged bands 1–2, 221–224, 104–113, and 148–167 are removed, 188 bands are reserved. This scene mainly contains a total of 12 materials which are Alunite, Andradite, Buddingtonite, Dumortierite, Kaolinite1, Kaolinite2, Muscovite, Montmorillonite, Nontronite, Pyrope, Sphene, and Chalcedony.

1) *Samson:* Fig. 8 shows a comparison between endmembers obtained by all tested algorithms from Samson data, where the soil endmembers obtained by SGSNMF, uDAS, and SNMF-Net have poorer effects, and those obtained by other algorithms have better effects. For tree endmember, all tested algorithms have achieved better results. However, ATGP-FCLS, HCSNMF-0.3, and HCSNMF-0.5 have achieved poor results on the water endmember, and other algorithms are

close to the reference (true) value. In particular, all three endmembers estimated by our SSAINMF perform well in Figs. 8 and 9.

Fig. 10 shows the abundance maps obtained by each algorithm on Samson. According to the reference abundance maps, there are few material types in Samson. With higher intraclass compactness, the distribution of each material type in Samson is concentrated. Such a feature is very suitable for the design of our SSAINMF. From the obtained abundances maps, ATGP-FCLS, HCSNMF-0.3, HCSNMF-0.5, uDAS,  $L_{1/2}$ NMF, MRSNMF, RNMF, MLNMF, MVNTF, and SNMF-Net all obtained poor abundance maps. However, SGSNMF and SSAINMF have better results. Especially since SSAINMF considers local similarity and removes the influence of band noise, it still obtains cleaner abundance maps and achieves the best results even when the initial values are not ideal.

TABLE III  
COMPARISON RESULTS OF EACH ALGORITHM ON JASPER RIDGE DATA

	NMSE ( $\times 10^{-2}$ )	RMSE	SAD				MSAD
			Tree	Water	Soil	Road	
ATGP-FCLS [10], [15]	31.0376	55.8361	0.1559	0.8953	0.1336	0.1069	0.3229
HCSNMF-0.3 [28]	0.3650	55.7570	0.1313	0.9228	0.0872	0.0601	0.3004
HCSNMF-0.5 [28]	0.3601	55.8222	0.1206	0.9036	0.1104	0.0628	0.2994
SGSNMF [24]	<b>0.2106</b>	48.4209	0.1021	<u>0.0611</u>	0.1132	0.0649	<u>0.0853</u>
uDAS [30]	1.5760	49.3684	0.2039	0.2965	0.1919	0.0854	0.1944
L1/2NMF [20]	0.2715	<u>46.6042</u>	0.1060	0.2771	0.1075	0.0646	0.1388
MRSNMF [22]	0.8876	<b>45.6652</b>	<b>0.0387</b>	0.2611	<b>0.0634</b>	0.0754	0.1096
RNMF [23]	0.7682	47.2179	0.0592	0.2372	0.0966	<u>0.0600</u>	0.1132
MLNMF [21]	1.1975	49.7801	<u>0.0474</u>	0.3964	<u>0.0637</u>	0.0633	0.1427
MVNNTF [35]	1.8961	66.6801	0.2771	0.1418	0.2150	0.1670	0.2002
SNMF-Net [36]	7.0328	57.5098	0.0999	0.1283	0.1103	0.0993	0.1095
Ours	<u>0.2134</u>	46.8760	0.0972	<b>0.0611</b>	0.1155	<b>0.0578</b>	<b>0.0829</b>

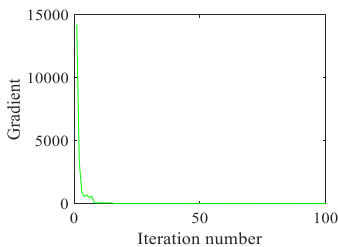


Fig. 14. Convergence curve of our SSAINMF on Jasper ridge data.

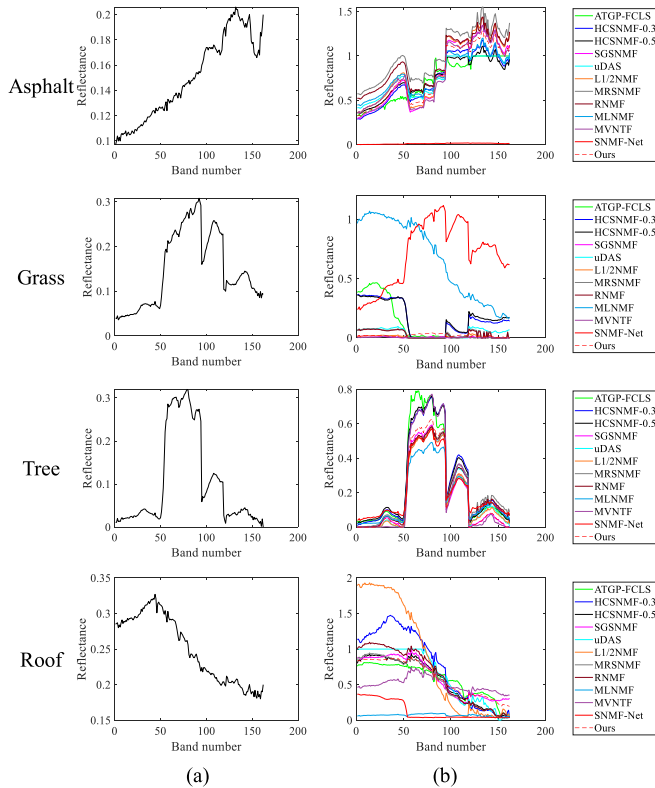


Fig. 15. Endmember curves evaluated by each algorithm on urban data. (a) True. (b) Estimate.

Table II shows the quantitative results of each tested algorithm on Samson data. In Table II, although

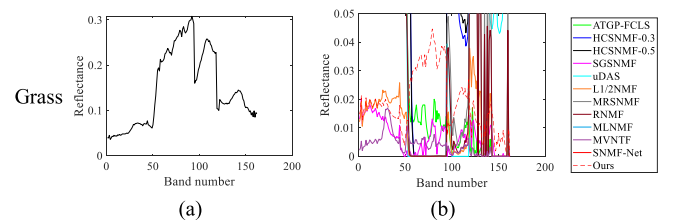


Fig. 16. Enlarged spectral curves of estimated water endmembers on urban data. (a) True. (b) Estimate.

HCSNMF-0.3, HCSNMF-0.5, and SGSNMF have better reconstruction effects, their abundance and endmember effects are poorer. The overall effects of ATGP-FCLS, MRSNMF, RNMF, and MLNMF are relatively poor. uDAS and MVNTF have better endmember effects, but they provide poorer abundance and reconstruction effects. SNMF-Net without better consideration of spectral information obtains poorer endmembers and abundances.  $L_{1/2}$ NMF with a sparse constraint obtains better endmembers, but its abundances are slightly poor. As a whole, although the reconstruction effect of our SSAINMF is not outstanding, it can be seen that SSAINMF provides not bad performance in all evaluation criteria. So, it achieves the better performance, with the best results for both abundance and endmembers.

Fig. 11 shows that the gradient of SSAINMF declines rapidly in the first five iterations, and then stabilizes, proving its good convergence.

2) *Jasper Ridge*: Fig. 12 shows a comparison of estimated endmembers from each tested algorithm with Jasper Ridge data. Among them, ATGP-FCLS, HCSNMF-0.3, and HCSNMF-0.5 obtain an incorrect Water spectral curve, indicating that HCSNMF-0.3 and HCSNMF-0.5 are more dependent on the setting of the initial value. The endmembers estimated by uDAS and MVNTF are better than those of ATGP-FCLS, HCSNMF-0.3, and HCSNMF-0.5, but are still inconsistent with the reference values. The endmembers evaluated by other algorithms are relatively close to the reference values and have achieved good results.

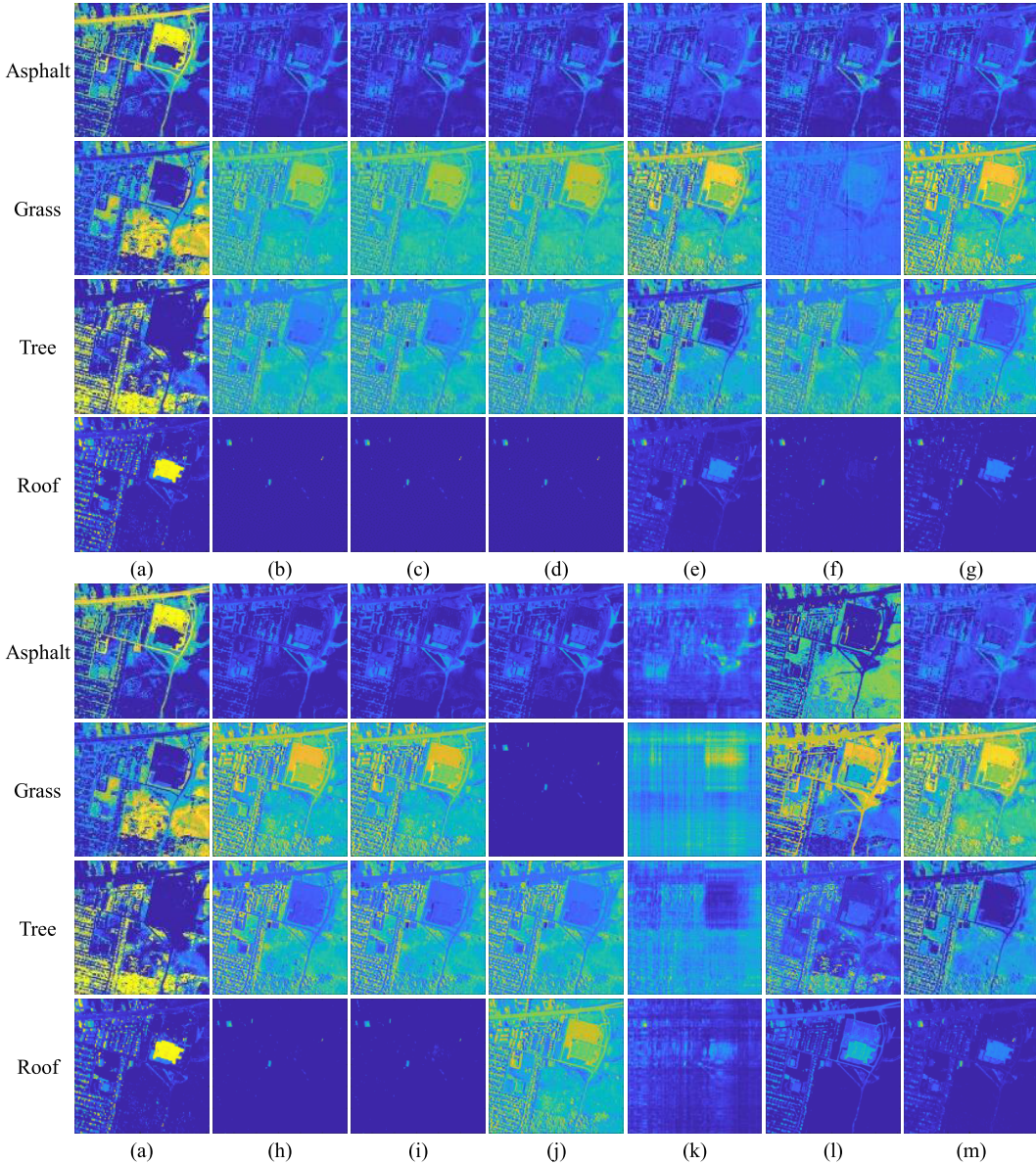


Fig. 17. Abundance maps evaluated by all tested algorithms with Urban data. (a) True. (b) ATGP-FCLS. (c) HCSNMF-0.3. (d) HCSNMF-0.5. (e) SGSNMF. (f) uDAS. (g)  $L_{1/2}$ NMF. (h) MRSNMF. (i) RNMF. (j) MLNMF. (k) MVNTF. (l) SNMF-Net. (m) Ours.

TABLE IV  
COMPARISON RESULTS OF EACH ALGORITHM ON URBAN DATA

	NMSE ( $\times 10^2$ )	RMSE	SAD				MSAD
			Asphalt	Grass	Tree	Roof	
ATGP-FCLS [10], [15]	27.9325	84.0658	0.1316	1.3665	<b>0.0743</b>	0.2174	0.4475
HCSNMF-0.3 [28]	0.4250	<u>83.3066</u>	0.1629	1.1837	0.1365	0.4002	0.4708
HCSNMF-0.5 [28]	1.2391	83.3087	<b>0.1029</b>	1.1607	0.1099	0.3391	0.4282
SGSNMF [24]	<b>0.3589</b>	84.5493	0.2287	0.9624	<u>0.1022</u>	0.2457	0.3848
uDAS [30]	2.8277	<b>83.2447</b>	0.1190	1.1802	0.1766	0.3530	0.4572
$L_1/2$ NMF [20]	0.7515	84.9194	0.2146	1.2233	0.1460	0.5445	0.5321
MRSNMF [22]	2.2271	90.3112	<u>0.1083</u>	1.2234	0.2146	0.3555	0.4755
RNMF [23]	1.9619	88.0273	0.1319	1.2567	0.1870	0.3763	0.4880
MLNMF [21]	3.5921	101.1174	0.1124	0.7421	0.1860	<u>0.2098</u>	0.3126
MVNTF [35]	8.8252	83.4461	0.2112	0.9354	0.1504	<b>0.1488</b>	0.3614
SNMF-Net [36]	173.8294	96.8961	0.2356	<b>0.1943</b>	0.1533	0.6648	<u>0.3120</u>
Ours	<u>0.4213</u>	85.7797	0.1853	<u>0.3749</u>	0.1103	0.2130	<b>0.2208</b>

TABLE V  
COMPARISON RESULTS OF EACH ALGORITHM ON CUPRITE DATA

	NMSE ( $\times 10^{-2}$ )	SAD											MSAD	
		Alunite	Andradite	Buddingtonite	Dumortierite	Kaolinite1	Kaolinite2	Muscovite	Montmorillonite	Nontronite	Pyrope	Sphene		
ATGP-FCLS [10], [15]	1.2744	<b>0.0859</b>	0.0994	0.1159	<b>0.0802</b>	0.0848	0.0852	<b>0.1027</b>	<b>0.0618</b>	<b>0.0736</b>	0.24	1.1329	0.0824	<b>0.1871</b>
HCSNMF-0.3 [28]	<b>0.0498</b>	0.0976	0.0824	0.16	0.1598	<b>0.0805</b>	<b>0.0637</b>	0.1793	0.0656	0.193	0.2376	1.1405	<b>0.0731</b>	0.2111
HCSNMF-0.5 [28]	<b>0.0519</b>	0.1577	0.2343	0.1963	0.1423	0.2617	<b>0.0622</b>	0.1981	0.0648	0.0797	0.5079	1.1428	0.1035	0.2626
SGSNMF [24]	2.1973	0.0949	0.998	1.225	0.1936	1.0767	0.2593	0.9622	0.0781	1.2937	0.5583	0.4677	0.261	0.6224
uDAS [30]	0.8079	0.2106	0.4773	<b>0.1159</b>	0.0804	0.1674	0.093	0.1464	<b>0.0562</b>	0.078	1.1105	0.1312	0.087	0.2295
L1/2NMF [20]	0.4776	0.1711	0.1887	0.251	0.0895	0.1097	0.1358	0.3141	0.0714	0.0793	<b>0.0751</b>	1.1871	0.0822	0.2296
MRSNMF [22]	0.473	0.1519	0.0812	0.1356	0.1081	0.1258	0.0802	0.1321	0.0641	<b>0.0768</b>	0.1138	1.119	<b>0.0781</b>	0.1889
RNMF [23]	0.4627	0.1573	0.082	0.3394	0.1143	0.1274	0.3988	1.1416	0.0658	0.0783	0.1871	<b>0.1105</b>	0.0815	0.2403
MLNMF [21]	0.6503	0.1367	<b>0.0789</b>	0.136	0.1498	0.1175	0.0722	0.1635	0.0639	0.0777	0.1353	1.1059	0.1319	0.1974
MVNNTF [35]	6.4966	0.1976	<b>0.0658</b>	0.3623	0.09	0.0828	0.0733	0.1191	0.0809	0.1375	0.1136	<b>0.0813</b>	1.501	0.2421
SNMF-Net [36]	54.9062	<b>0.0857</b>	0.0853	0.1583	<b>0.0802</b>	<b>0.0814</b>	0.093	<b>0.1027</b>	0.0628	0.1144	1.1266	0.8705	0.0862	0.2456
Ours	0.3903	0.0994	0.1055	<b>0.1074</b>	0.0831	0.1247	0.0822	0.2825	0.0663	0.0769	<b>0.0644</b>	1.0495	0.087	<b>0.1857</b>

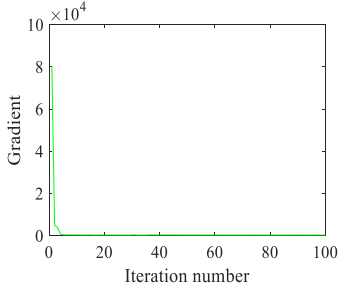


Fig. 18. Convergence curve of our SSAINMF on urban data.

Fig. 13 shows the abundance maps evaluated by each algorithm on Jasper Ridge. From the obtained abundance results, ATGP-FCLS, HCSNMF-0.3, and HCSNMF-0.5 misidentify the water endmembers as the road endmembers, so that the road abundances are wrongly distributed in the water abundance maps. However, this situation is improved in SGSNMF,  $L_{1/2}$ NMF, SNMF-Net, and SSAINMF, proving that they perform better.

Table III gives the quantitative results of each algorithm on Jasper Ridge data, in which ATGP-FCLS, HCSNMF-0.3, and HCSNMF-0.5 perform the worst. The abundance effect of uDAS is better, but its reconstruction and endmembers effects are poor. The reconstruction and abundance errors of MVNTF and SNMF-Net are larger. In contrast, SGSNMF, MRSNMF, RNMF, and our SSAINMF perform better. However, SGSNMF, MRSNMF, and RNMF ignore the influence of band noise, so their results are slightly worse than SSAINMF.

Since the 16th iteration, the gradient of SSAINMF has been stable in Fig. 14.

3) *Urban*: A comparison of endmembers obtained by each algorithm on urban data is shown in Fig. 15. It can be found that the asphalt, tree, and roof spectral curves estimated by most algorithms are relatively close to the reference values. However, the estimation of grass endmembers is challenging, and most algorithms achieve a poor spectral

curve. On the contrary, the grass endmembers evaluated by SSAINMF and SNMF-Net are very close to the reference value in Figs. 15 and 16, and the effects are better, but SNMF-Net obtains a poor Roof endmember. Fig. 17 shows the abundance maps evaluated by each algorithm on urban. The abundances obtained by each algorithm are poor, but in SGSNMF,  $L_{1/2}$ NMF, SNMF-Net, and SSAINMF, the roof abundances are improved.

Table IV summarizes the quantitative results of each algorithm for urban data. It can be found that the overall performance of ATGP-FCLS is poor, and the reconstruction error is larger. The estimated abundances and endmembers of MRSNMF, RNMF, MLNMF, and SNMF-Net are unreliable. The endmembers extracted by HCSNMF-0.3, HCSNMF-0.5, SGSNMF, uDAS,  $L_{1/2}$ NMF, and MVNTF are less effective. Although the abundances estimated by SSAINMF are slightly worse, its reconstruction and endmember effects are very good. In particular, the endmembers it extracts have achieved the first good result.

From Fig. 18, the gradient of SSAINMF on urban soon declines and then stabilizes.

4) *Cuprite*: Fig. 19 shows the comparison of the endmember spectra obtained by each algorithm on Cuprite data. Among them, the Andradite, Buddingtonite, Kaolinite1, Nontronite, and Pyrope endmember curves estimated by SGSNMF are less effective, and those estimated by other algorithms are more effective.  $L_{1/2}$ NMF and SSAINMF provides advantages in estimating Pyrope endmembers. In the optimization process, they better compensate for the deviations of the initial values. Moreover, since cuprite has no abundance ground truth, only the abundance maps of SSAINMF are shown in Fig. 20. It can be found that the sparsity of its abundances is better.

Table V shows the quantitative results of each algorithm on cuprite data, and the endmember and reconstruction effects of SGSNMF are both poor. The endmember effects of ATGP-FCLS are better, but its reconstruction performance is poor. The reconstruction performance of HCSNMF-0.3 and

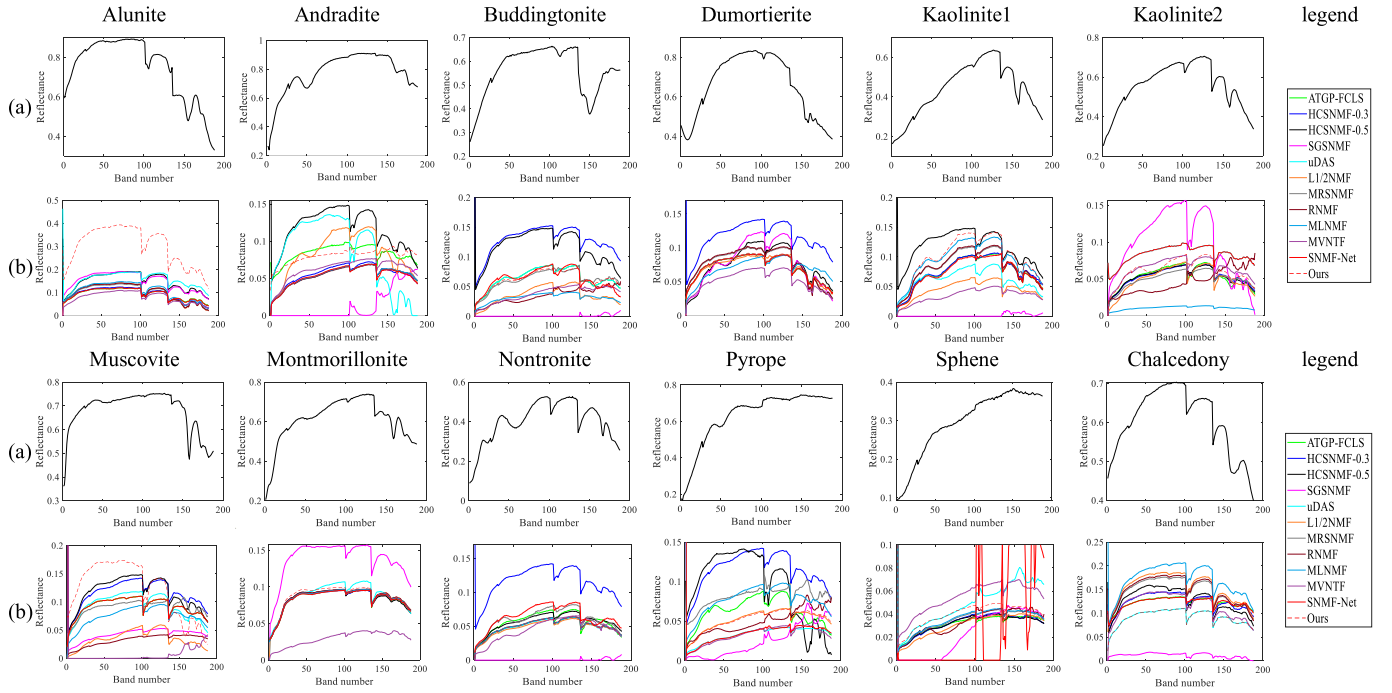


Fig. 19. Endmember curves evaluated by each algorithm on the Cuprite data. (a) True. (b) Estimate.

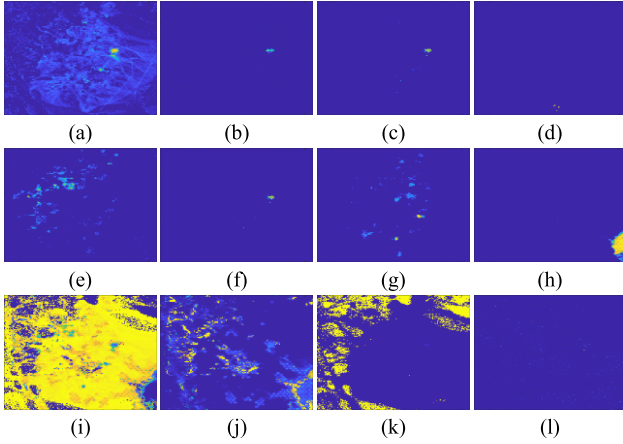


Fig. 20. Abundance maps evaluated by our SSAINMF with cuprite data. (a) Alunite. (b) Andradite. (c) Buddingtonite. (d) Dumortierite. (e) Kaolinite1. (f) Kaolinite2. (g) Muscovite. (h) Montmorillonite. (i) Nontronite. (j) Pyrope. (k) Sphene. (l) Chalcedony.

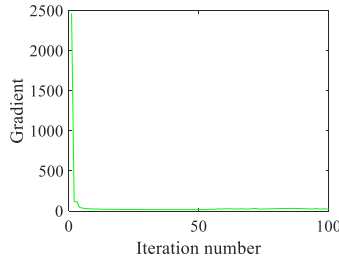


Fig. 21. Convergence curve of our SSAINMF on Cuprite data.

HCSNMF-0.5 is the best, but their endmember effects are slightly worse. In contrast, the estimated endmembers of SSAINMF achieve the best results in the case of smaller reconstruction errors, and its performance is better. Fig. 21

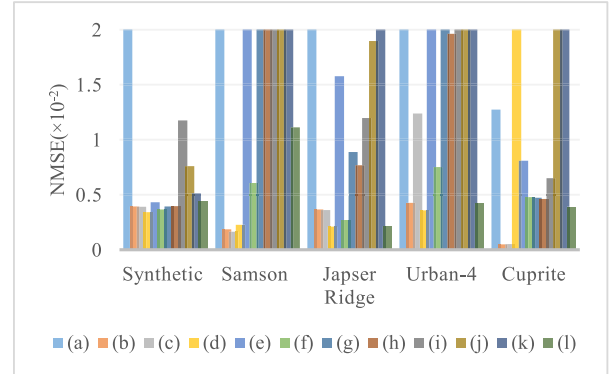


Fig. 22. Reconstruction performance of each algorithm on five datasets. (a) ATGP-FCLS. (b) HCSNMF-0.3. (c) HCSNMF-0.5. (d) SGSNMF. (e) uDAS. (f)  $L_{1/2}$ NMF. (g) MRSNMF. (h) RNMF. (i) MLNMF. (j) MVNTF. (k) SNMF-Net. (l) Ours.

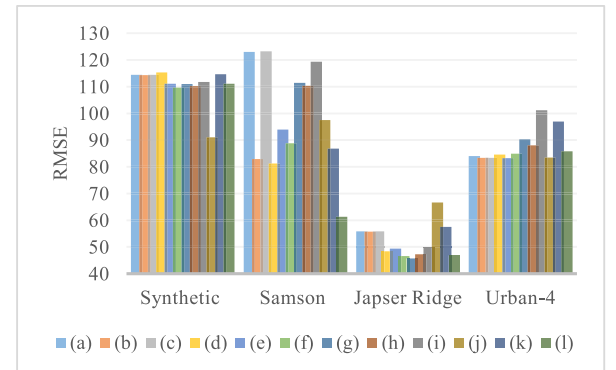


Fig. 23. Abundance performance of each algorithm on four datasets. (a) ATGP-FCLS. (b) HCSNMF-0.3. (c) HCSNMF-0.5. (d) SGSNMF. (e) uDAS. (f)  $L_{1/2}$ NMF. (g) MRSNMF. (h) RNMF. (i) MLNMF. (j) MVNTF. (k) SNMF-Net. (l) Ours.

illustrates that the gradient of SSAINMF declines rapidly in the first five iterations, and then becomes stable.

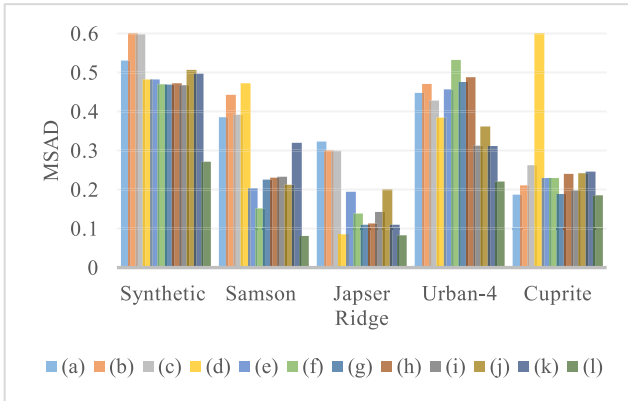


Fig. 24. Endmember performance of each algorithm on five datasets. (a) ATGP-FCLS. (b) HCSNMF-0.3. (c) HCSNMF-0.5. (d) SGSNMF. (e) uDAS. (f)  $L_{1/2}$ NMF. (g) MRSNMF. (h) RNMF. (i) MLNMF. (j) MVNTF. (k) SNMF-Net. (l) Ours.

On the whole, Figs. 22–24 show the comparison histograms of the reconstruction, abundance, and endmember effects of 12 tested algorithms on different data, respectively. It can be seen that the proposed SSAINMF can achieve better endmembers and abundances from the transformed spaces of synthetic and real data without high reconstruction error.

## V. CONCLUSION

As is well known, external interference brings serious challenges to spectral unmixing. To effectively improve the unmixing robustness, this article develops a spectral-spatial anti-interference NMF for hyperspectral unmixing, named SSAINMF. On the one hand, we focus on the effectiveness of the band information. Because endmember estimation involves all bands, the damaged bands directly affect the spectral information of the estimated endmembers. To this end, the priority bands of statistical components within the data are first defined by transforming the original data space. According to the contribution of each priority band, their weights are quantified, so as to effectively repair damaged information in original space during optimization. Most importantly, we also demonstrate the restricted isometric and restricted isospectral properties for abundances and endmembers between the original domain and the transformation domain, which provides the basis for spectral unmixing based on spatial transformations in the future. On the other hand, we also consider the high homogeneity within a neighborhood. A set of inductive indices are first introduced to control the structural sparsity of the abundances in the neighborhood. A pixel similarity constraint is also designed to further guarantee the spatial smoothness of pixels in the neighborhood. At the same time, the similarity degree between these pixels is also controlled by using the spatial-spectral distance indices. This not only enhances the resistance to interference, such as spatial noise and spectral variability but also effectively promotes the idealization of estimated endmember spectra.

In short, combining with the better performance on synthetic and real data, it can be observed that SSAINMF can, indeed, reduce the interference such as noise and spectral variability by considering the effects of both band and spatial information.

In particular, in large homogeneous regions, the advantages of band priorities and spatial similarity can be fully exploited. Under effectively resisting the false guidance of the initial values, SSAINMF can deeply mine the clean components in a homogeneous region, and characterize the endmember and abundance information adaptively and effectively.

## ACKNOWLEDGMENT

The authors would like to thank Dr. Fengchao Xiong for providing the source code and data of SNMF-Net for experiments.

## REFERENCES

- [1] F. Li, M. Song, B. Xue, and C. Yu, "Abundance estimation based on band fusion and prioritization mechanism," *IEEE Trans. Geosci. Remote Sens.*, vol. 60, 2022, Art. no. 5532621.
- [2] Z. Han, D. Hong, L. Gao, B. Zhang, M. Huang, and J. Chanussot, "AutoNAS: Automatic neural architecture search for hyperspectral unmixing," *IEEE Trans. Geosci. Remote Sens.*, vol. 60, 2022, Art. no. 5532214.
- [3] T. Chen, Y. Liu, Y. Zhang, B. Du, and A. Plaza, "Superpixel-based collaborative and low-rank regularization for sparse hyperspectral unmixing," *IEEE Trans. Geosci. Remote Sens.*, vol. 60, 2022, Art. no. 5529216.
- [4] Z. Han, D. Hong, L. Gao, S. K. Roy, B. Zhang, and J. Chanussot, "Reinforcement learning for neural architecture search in hyperspectral unmixing," *IEEE Geosci. Remote Sens. Lett.*, vol. 19, pp. 1–5, 2022.
- [5] G. Zhang, P. Scheunders, D. Cerra, and R. Müller, "Shadow-aware nonlinear spectral unmixing for hyperspectral imagery," *IEEE J. Sel. Topics Appl. Earth Observ. Remote Sens.*, vol. 15, pp. 5514–5533, 2022.
- [6] J. W. Boardman, "Automating spectral unmixing of AVIRIS data using convex geometry concepts," in *Proc. Summaries 4th Annu. JPL Airborne Geosci. Workshop (AVIRIS Workshop)*, vol. 26, no. 1, 1993, pp. 11–14.
- [7] J. Boardman, F. A. Kruse, and R. O. Green, "Mapping target signatures via partial unmixing of AVIRIS data," in *Proc. JPL Airborne Earth Sci. Workshop*, vol. 1, R. O. Green, Ed. 1995, pp. 23–26.
- [8] J. M. P. Nascimento and J. M. B. Dias, "Vertex component analysis: A fast algorithm to unmix hyperspectral data," *IEEE Trans. Geosci. Remote Sens.*, vol. 43, no. 4, pp. 898–910, Apr. 2005.
- [9] M. E. Winter, "N-FINDR: An algorithm for fast autonomous spectral end-member determination in hyperspectral data," *Proc. SPIE*, vol. 3753, pp. 266–275, Oct. 1999.
- [10] H. Ren and C.-I Chang, "Automatic spectral target recognition in hyperspectral imagery," *IEEE Trans. Aerosp. Electron. Syst.*, vol. 39, no. 4, pp. 1232–1249, Oct. 2003.
- [11] C.-I Chang, C.-C. Wu, W. Liu, and Y.-C. Ouyang, "A new growing method for simplex-based endmember extraction algorithm," *IEEE Trans. Geosci. Remote Sens.*, vol. 44, no. 10, pp. 2804–2819, Oct. 2006.
- [12] C.-I Chang, C.-C. Wu, K.-H. Liu, H.-M. Chen, C. C. Chen, and C.-H. Wen, "Progressive band processing of linear spectral unmixing for hyperspectral imagery," *IEEE J. Sel. Topics Appl. Earth Observ. Remote Sens.*, vol. 8, no. 6, pp. 2583–2597, Jun. 2015.
- [13] C.-I Chang and D. C. Heinz, "Constrained subpixel target detection for remotely sensed imagery," *IEEE Trans. Geosci. Remote Sens.*, vol. 38, no. 3, pp. 1144–1159, May 2000.
- [14] C.-I Chang, *Hyperspectral Imaging: Techniques for Spectral Detection and Classification*. New York, NY, USA: Springer, 2003.
- [15] D. C. Heinz and Chein-I-Chang, "Fully constrained least squares linear spectral mixture analysis method for material quantification in hyperspectral imagery," *IEEE Trans. Geosci. Remote Sens.*, vol. 39, no. 3, pp. 529–545, Mar. 2001.
- [16] A. Einizade and S. H. Sardouie, "A unified approach for simultaneous graph learning and blind separation of graph signal sources," *IEEE Trans. Signal Inf. Process. over Netw.*, vol. 8, pp. 543–555, 2022.
- [17] D. D. Lee and H. S. Seung, "Learning the parts of objects by non-negative matrix factorization," *Nature*, vol. 401, no. 6755, pp. 788–791, Oct. 1999.
- [18] L. Miao and H. Qi, "Endmember extraction from highly mixed data using minimum volume constrained nonnegative matrix factorization," *IEEE Trans. Geosci. Remote Sens.*, vol. 45, no. 3, pp. 765–777, Mar. 2007.

- [19] Z. Guo, A. Min, B. Yang, J. Chen, H. Li, and J. Gao, “A sparse oblique-manifold nonnegative matrix factorization for hyperspectral unmixing,” *IEEE Trans. Geosci. Remote Sens.*, vol. 60, 2022, Art. no. 5508013.
- [20] Y. Qian, S. Jia, J. Zhou, and A. Robles-Kelly, “Hyperspectral unmixing via  $L_{1/2}$  sparsity-constrained nonnegative matrix factorization,” *IEEE Trans. Geosci. Remote Sens.*, vol. 49, no. 11, pp. 4282–4297, Nov. 2011.
- [21] R. Rajabi and H. Ghassemian, “Spectral unmixing of hyperspectral imagery using multilayer NMF,” *IEEE Geosci. Remote Sens. Lett.*, vol. 12, no. 1, pp. 38–42, Jan. 2015.
- [22] X. Lu, H. Wu, Y. Yuan, P. Yan, and X. Li, “Manifold regularized sparse NMF for hyperspectral unmixing,” *IEEE Trans. Geosci. Remote Sens.*, vol. 51, no. 5, pp. 2815–2826, May 2013.
- [23] L. Tong, J. Zhou, X. Li, Y. Qian, and Y. Gao, “Region-based structure preserving nonnegative matrix factorization for hyperspectral unmixing,” *IEEE J. Sel. Topics Appl. Earth Observ. Remote Sens.*, vol. 10, no. 4, pp. 1575–1588, Apr. 2017.
- [24] X. Wang, Y. Zhong, L. Zhang, and Y. Xu, “Spatial group sparsity regularized nonnegative matrix factorization for hyperspectral unmixing,” *IEEE Trans. Geosci. Remote Sens.*, vol. 55, no. 11, pp. 6287–6304, Nov. 2017.
- [25] Y. Yuan, Z. Zhang, and Q. Wang, “Improved collaborative non-negative matrix factorization and total variation for hyperspectral unmixing,” *IEEE J. Sel. Topics Appl. Earth Observ. Remote Sens.*, vol. 13, pp. 998–1010, 2020.
- [26] S. Zhang et al., “Spectral–spatial hyperspectral unmixing using nonnegative matrix factorization,” *IEEE Trans. Geosci. Remote Sens.*, vol. 60, 2022, Art. no. 5505713.
- [27] X. Li, R. Huang, and L. Zhao, “Correntropy-based spatial–spectral robust sparsity-regularized hyperspectral unmixing,” *IEEE Trans. Geosci. Remote Sens.*, vol. 59, no. 2, pp. 1453–1471, Feb. 2021.
- [28] Z. Wang, M. He, L. Wang, K. Xu, J. Xiao, and Y. Nian, “Semi-NMF-based reconstruction for hyperspectral compressed sensing,” *IEEE J. Sel. Topics Appl. Earth Observ. Remote Sens.*, vol. 13, pp. 4352–4368, 2020.
- [29] J. Peng, Y. Zhou, W. Sun, Q. Du, and L. Xia, “Self-paced nonnegative matrix factorization for hyperspectral unmixing,” *IEEE Trans. Geosci. Remote Sens.*, vol. 59, no. 2, pp. 1501–1515, Feb. 2021.
- [30] Y. Qu and H. Qi, “UDAS: An untied denoising autoencoder with sparsity for spectral unmixing,” *IEEE Trans. Geosci. Remote Sens.*, vol. 57, no. 3, pp. 1698–1712, Mar. 2019.
- [31] A. Bekht, C.-I Chang, B. Lampe, C. J. D. Porta, and C.-C. Wu, “N-FINDER for finding endmembers in compressively sensed band domain,” *IEEE Trans. Geosci. Remote Sens.*, vol. 58, no. 2, pp. 1087–1101, Feb. 2020.
- [32] J. C. Harsanyi and C.-I Chang, “Hyperspectral image classification and dimensionality reduction: An orthogonal subspace projection approach,” *IEEE Trans. Geosci. Remote Sens.*, vol. 32, no. 4, pp. 779–785, Jul. 1994.
- [33] C.-I Chang, H. Cao, S. Chen, X. Shang, C. Yu, and M. Song, “Orthogonal subspace projection-based go-decomposition approach to finding low-rank and sparsity matrices for hyperspectral anomaly detection,” *IEEE Trans. Geosci. Remote Sens.*, vol. 59, no. 3, pp. 2403–2429, Mar. 2021.
- [34] R. Achanta, A. Shaji, K. Smith, A. Lucchi, P. Fua, and S. Süsstrunk, “SLIC superpixels compared to state-of-the-art superpixel methods,” *IEEE Trans. Pattern Anal. Mach. Intell.*, vol. 34, no. 11, pp. 2274–2282, Nov. 2012.
- [35] Y. Qian, F. Xiong, S. Zeng, J. Zhou, and Y. Y. Tang, “Matrix-vector nonnegative tensor factorization for blind unmixing of hyperspectral imagery,” *IEEE Trans. Geosci. Remote Sens.*, vol. 55, no. 3, pp. 1776–1792, Mar. 2017.
- [36] F. Xiong, J. Zhou, S. Tao, J. Lu, and Y. Qian, “SNMF-Net: Learning a deep alternating neural network for hyperspectral unmixing,” *IEEE Trans. Geosci. Remote Sens.*, vol. 60, 2022, Art. no. 5510816.



**Tingting Yang** received the B.S. and M.S. degrees in communication engineering and computer technology from Liaoning Shihua University, Fushun, China, in 2016 and 2020, respectively. She is currently pursuing the Ph.D. degree in information and communication engineering with Dalian Maritime University, Dalian, China.

Her research interests include hyperspectral image unmixing and applications.



**Meiping Song** (Member, IEEE) received the Ph.D. degree from the College of Computer Science and Technology, Harbin Engineering University, Harbin, China, in 2006.

From 2013 to 2014, she was a Visiting Associate Research Scholar with the Remote Sensing Signal and Image Processing Laboratory, University of Maryland, Baltimore County, Baltimore, MD, USA. Since 2006, she has been with Dalian Maritime University, Dalian, China, where she is currently a Professor with the College of Information Science and Technology. Her research interests include remote sensing and hyperspectral image processing.



**Sen Li** received the B.S. degree in microelectronics from Liao Ning University, Shenyang, China, in 1996, the M.S. degree in information and communication engineering from Dalian Maritime University, Dalian, China, in 1999, and the Ph.D. degree in information and signal processing from the Dalian University of Technology, Dalian, in 2011.

In 2013, she held a post-doctoral position at the Department of Electrical and Computer Engineering, Concordia University, Montreal, QC, Canada. She is currently a Professor with the Department of Information Science and Technology, Dalian Maritime University. Her research interests include spectral estimation, array signal processing, communication signal processing, statistics and adaptive signal processing, and non-Gaussian signal processing.



**Yulei Wang** (Member, IEEE) was born in Yantai, Shandong, China, in 1986. She received the B.S. and Ph.D. degrees in signal and information processing from Harbin Engineering University, Harbin, China, in 2009 and 2015, respectively.

She is currently an Associate Professor and a Doctoral Supervisor with the Center for Hyperspectral Imaging in Remote Sensing (CHIRS), Information Science and Technology College, Dalian Maritime University, Dalian, China. Her research interests include hyperspectral image (HSI) processing and vital signs signal processing.

Dr. Wang was awarded by the China Scholarship Council in 2011 as a joint Ph.D. student to study at the Remote Sensing Signal and Image Processing Laboratory, University of Maryland, Baltimore County, Baltimore, MD, USA, for two years.